

1 **Shallow Slow Earthquake Episodes Near the Trench Axis Off Costa Rica**

2

3 **Satoru Baba¹, Kazushige Obara¹, Shunsuke Takemura¹, Akiko Takeo¹, and Geoffrey A.**
4 **Abers²**

5 ¹Earthquake Research Institute, The University of Tokyo, Tokyo, Japan

6 ²Department of Earth and Atmospheric Sciences, Cornell University, Ithaca, New York, United
7 States of America

8

9 Corresponding author: Satoru Baba (babasatoru@eri.u-tokyo.ac.jp)

10

11 **Key Points:**

- 12 • Shallow very low frequency earthquakes (VLFEs) and tremors are detected off Costa
13 Rica near the Middle America Trench
- 14 • Distribution of VLFEs and tremors is spatially correlated with slow slip events
- 15 • Scaled energy of shallow slow earthquakes off Costa Rica is 10^{-9} – 10^{-8} , which is similar to
16 those in Nankai

17

18 **Abstract**

19 Slow earthquakes are mainly distributed in regions surrounding seismogenic zones
20 along the plate boundaries of subduction zones. In the Central American subduction zone, large
21 regular interplate earthquakes with magnitudes of 7–8 occur repeatedly around the Nicoya
22 Peninsula, in Costa Rica, and a tsunami earthquake occurred off Nicaragua, just north of Costa
23 Rica, in 1992. To clarify the spatial distribution of various slip behaviors at the plate boundary, we
24 detected and located very low frequency earthquakes (VLFs) around the Nicoya Peninsula using
25 a grid-search matched-filter technique with synthetic templates based on a regional three-
26 dimensional model. VLFs were active in September 2004 and August 2005, mainly near the
27 trench axis, updip of the seismogenic zone. The distribution of VLFs overlaps with large slip
28 areas of slow slip events. Low frequency tremor signals were also found in high-frequency
29 seismogram envelopes within the same time windows as detected VLFs; thus, we also
30 investigated the energy rates of tremors accompanied by VLFs. The range of scaled energy,
31 which is the ratio of the seismic energy rate of a tremor to the seismic moment rate of
32 accompanying VLF and related to the rupture process of seismic phenomena, was 10^{-9} – 10^{-8} . The
33 along-dip separation of shallow slow and large earthquakes and the range of the scaled energy off
34 Costa Rica are similar to those in shallow slow earthquakes in Nankai, which shares a similar
35 thermal structure along the shallow plate boundary.

36 **Plain language summary**

37 Slow earthquakes with slower rupture speeds compared to those of regular earthquakes
38 generally occur on the plate boundaries of subduction zones. We detected and located very low
39 frequency earthquakes (VLFs), which are a type of slow earthquake, off Costa Rica. The VLFs
40 occurred at a depth range of 6–10 km, and their spatial distribution is correlated with slow slip
41 events, another type of slow earthquakes. The spatial separation of slow and large regular
42 earthquakes is common to the Nankai subduction zone. Low frequency tremor signals, which are
43 also classified as slow earthquakes, are also found in seismograms at higher frequencies within the
44 same time windows of detected VLFs. We also estimated the ratio of energy rates of tremors to
45 moment rates of VLFs, which relates to the rupture process of seismic phenomena. The ratio is
46 10^{-9} – 10^{-8} off Costa Rica, similar to that in shallow slow earthquakes in the Nankai subduction zone.

47 **1. Introduction**

48 Slow earthquakes are mainly observed in regions surrounding seismogenic zones, which
49 are the areas that rupture in large regular earthquakes, along the plate boundaries of subduction
50 zones (e.g., Obara & Kato, 2016) or strike-slip faults (e.g., Nadeau & Dolenc, 2005; Wang &
51 Barbot, 2020). Various types of slow earthquakes, such as low frequency tremors (tectonic
52 tremors; e.g., Obara, 2002), low frequency earthquakes (LFs; e.g., Shelly et al., 2006), very low
53 frequency earthquakes (VLFs; e.g., Obara & Ito, 2005), and slow slip events (SSEs; e.g., Dragert
54 et al., 2001) have been observed in many subduction zones. Although these slow earthquake
55 phenomena occur without correlation in some cases (Hutchison, 2020; Hutchison & Ghosh, 2016,
56 2019), they often correlate spatiotemporally, which is termed episodic tremor and slip (ETS). ETSs
57 were observed in deep Cascadia (e.g., Ghosh et al., 2015; Rogers & Dragert, 2003) and deep
58 Nankai (e.g., Ito et al., 2007; Obara, 2011), for example. Recently, in the Nankai subduction zone,
59 pore fluid pressure changes have been observed during tremor and VLF activities and are
60 considered to reflect shallow SSEs by offshore borehole observations (Araki et al., 2017; Nakano

61 et al., 2018). The hypocenters and focal mechanisms of slow earthquakes are generally consistent
62 with shear slip on the plate boundaries. VLFE episodes and SSEs occur in almost identical source
63 regions and their temporal changes of moment release are similar during as ETS, therefore VLFE
64 episodes are considered as proxies for SSEs (Ghosh et al., 2015; Ito et al., 2007; Nakano et al.,
65 2018; Yokota & Ishikawa, 2020). In summary, the distribution of slow earthquakes is related to
66 large earthquake slip areas, interplate coupling, or fluid distribution (e.g., Baba et al., 2020b;
67 Ghosh et al., 2015; Obara & Kato, 2016).

68 In the Central American subduction zone, the Cocos plate subducts beneath the Caribbean
69 plate at the Middle America Trench at a rate of approximately 80 mm/year (Figure 1b; referred
70 from NUVEL1A; DeMets et al., 1994). In this subduction zone, large thrust-type earthquakes with
71 a moment magnitude (M_w) of 7–8 occur with a recurrence interval of tens of years around the
72 Nicoya Peninsula, in Costa Rica (light blue areas in Figure 1a; Protti, 1995; Yue et al., 2013). The
73 coseismic slip areas of these large earthquakes are distributed at a depth range of 10–35 km beneath
74 the peninsula and off the coast. The latest large earthquake with M_w of 7.6 occurred on 5
75 September, 2012 (green contour lines in Figure 1a; Yue et al., 2013). In the vicinity, a tsunami
76 earthquake with M_w of 7.6 also occurred off Nicaragua, just north of Costa Rica, on 2 September,
77 1992 (dark blue area in Figure 1a; Satake, 1994).

78 In addition to large regular and tsunami earthquakes, slow earthquakes also occur around
79 the Nicoya Peninsula. The Global Navigation Satellite System data revealed that SSEs with M_w
80 of 6.6–7.2 occur at intervals of 21.7 ± 2.6 months (Jiang et al., 2012; Xie et al., 2020). The large
81 slip area of the SSE in 2007 was separated into downdip and updip areas by the seismogenic slip
82 area (Jiang et al., 2012, 2017; Outerbridge et al., 2010). The spatiotemporal change in relation to
83 the 2012 M_w 7.6 earthquake was investigated by previous studies (Dixon et al., 2014; Voss et al.,
84 2017), and an SSE preceded the 2012 M_w 7.6 earthquake (Voss et al., 2018) in the almost same
85 area of the 2007 SSE, similar to both the slow slip before the 2011 Tohoku earthquake in Japan
86 (Ito et al., 2013; Kato et al., 2012) and the slow slip before the 2014 Iquique earthquake in Chile
87 (Kato & Nakagawa, 2014; Ruiz et al., 2017).

88 By using high-frequency (>1 Hz) seismograms, Brown et al. (2009) and Outerbridge et al.
89 (2010) located LFEs and tremors in 2007, respectively (Figure 1a). The tremors and LFEs were
90 located in almost the same area, downdip of the seismogenic zone. Although tremors and LFEs
91 were temporally correlated with the SSE, the location of tremors and LFEs were separated from
92 the large slip area of the 2007 SSE. On the other hand, Walter et al. (2011) located many tremors
93 in the offshore region from 2007 to 2009. Walter et al. (2013) also found that VLFs appeared in
94 seismograms in a frequency range of 0.02–0.05 Hz and were temporally correlated with tremors
95 in the time period of the 2008 SSE. Based on beamforming analysis, they estimated the propagation
96 direction and the propagation speed of VLFE signals and suggested that VLFs also occurred in
97 offshore areas. Due to the limitations of a conventional analysis, however, epicenters of VLFs in
98 offshore areas were not located. Therefore, the detailed spatial distribution of VLFs off Costa
99 Rica is still not well understood.

100 The spatial variation of slow and large regular earthquakes can reflect the spatial
101 heterogeneity of the frictional conditions on the plate boundary (e.g., Baba et al., 2020b). To clarify
102 the spatial relationship between slow and large regular earthquake distribution around the Nicoya
103 Peninsula, an accurate spatial distribution of VLFs is needed. Thus, we detected VLFs around
104 the Nicoya Peninsula using a temporary broadband seismic network from August 2004 to January
105 2006 because signals of VLFs are less attenuated than those of tremors and propagate longer

106 distances. The method is based on the matched-filter technique. Template waveforms from
107 possible VLFE locations were evaluated by numerical simulations of seismic wave propagation
108 using a regional three-dimensional (3D) velocity structure model. In addition, scaled energy is an
109 informative parameter for the rupture process of seismic phenomena (Kanamori & Rivera, 2006).
110 Although scaled energies of slow earthquakes around Japan were well investigated by previous
111 studies (e.g., Ide & Yabe, 2014; Yabe et al., 2019; 2021), those in Costa Rica was not estimated.
112 Therefore, we also estimated the seismic energy rate functions of tremors accompanied by VLFES
113 by using high frequency (2–8 Hz) seismograms to evaluate the scaled energy of slow earthquakes
114 around the Nicoya Peninsula.

115 **2. VLFE analysis**

116 **2.1. Data and method**

117 **2.1.1. Data**

118 We used waveforms of a temporary seismic network, Tomography Under Costa Rica and
119 Nicaragua (TUCAN; Abers & Fischer, 2003), recorded from August 2004 to January 2006. There
120 were 49 broadband seismic stations in four lines (Figure 1b). In this study, we mainly used data
121 from stations in Costa Rica (shown in Figure 1a) for VLFE analysis. After removing instrumental
122 responses, the seismograms for VLFE detection were resampled at one sample per second. We
123 applied a bandpass filter in the frequency range of 0.02–0.05 Hz (e.g., Ghosh et al., 2015; Ito et
124 al., 2009; Takemura et al., 2019), because this frequency band is less affected by microseismic
125 noises (e.g., Hasselmann, 1963; Kaneko et al., 2018). We verified that the large amplitude surface
126 waves are generally matched well between observed and synthetic waveforms in a higher
127 frequency range (Figure S1; 0.02-0.06 Hz).

128 **2.1.2. Matched-filter technique**

129 The detection procedure used for VLFES is similar to that used in our previous study (Baba
130 et al., 2020a). We used only the vertical component seismograms because the horizontal
131 component seismograms of many stations were noisy, and it was difficult to find VLFE signals
132 (Figure S2). We placed 175 virtual source grids on the Cocos Plate boundary at a uniform interval
133 of 0.1° (Figure 2a) and computed synthetic waveforms from these source grids to the stations in
134 Costa Rica using an open-source seismic wave propagation code (OpenSWPC; Maeda et al., 2017).
135 We used a three-dimensional velocity structure model constructed by combining CRUST 1.0
136 (Laske et al., 2013), Slab2 (Hayes et al., 2018), and ETOPO1 (Amante & Eakins, 2009), setting
137 the minimum S-wave velocity in the solid columns to 1.0 km/s. We adopted the values of a mean
138 oceanic slab structure (Christensen & Salisbury, 1975) for the physical parameters of the
139 subducting slab (Table S1). For the physical parameters of the other layers except for the slab, we
140 used the values of CRUST 1.0, and the default parameter set of OpenSWPC. The model covered
141 the region enclosed by the red line (Figure 1b), which was discretized by a uniform grid interval
142 of 0.2 km. The assumed VLFE moment rate function was a Küpper wavelet with a source duration
143 of 15 s and an M_w of 4.0 (Figure 4 of Maeda et al., 2017). Since focal mechanisms of VLFES are
144 consistent with shear slip on the plate boundaries in previous studies (Cascadia: Ghosh et al., 2015;
145 Nankai: Ito et al., 2009; Nakano et al., 2018; Sugioka et al., 2012; Takemura et al., 2019), the focal
146 mechanism at each source grid was assumed to be consistent with the geometry of the plate
147 boundary of Slab2 and the plate motion model, NUVEL-1A (DeMets et al., 1994). The time
148 window of each template was set to 150 s from the event origin time. Hereafter, we simply refer
149 to these synthetic waveforms as template waveforms. Examples of template waveforms at updip

150 and downdip source grids are shown in Figures 2b and 2c, respectively. The signal first arrives at
 151 MANS and the variation of amplitudes is small for the updip source, whereas signals first arriving
 152 at FINA exhibit amplitudes in or near the Nicoya Peninsula that are much larger than in other areas
 153 for the downdip source.

154 We then calculated cross-correlation coefficients (CCs) between the filtered template
 155 waveforms and observed seismograms every 1 s. We selected events with station-averaged
 156 coefficients larger than a threshold defined as 9.5 times the median absolute deviation (MAD) of
 157 the distributions. In order to decrease false detections by non-VLFE signals on the condition that
 158 only the vertical component can be used and the station coverage along the azimuth direction is
 159 poor, we adopted a strict detection threshold compared to previous studies (e.g., $8 \times \text{MAD}$ in Shelly
 160 et al., 2007 and Baba et al., 2018 and $9 \times \text{MAD}$ in Baba et al., 2020a). The changes of CCs when
 161 focal mechanisms or depths of assumed source models are different from the geometry of the plate
 162 boundary are shown in Figure S3.

163 2.1.3. VLFE location and discarding false detections

164 Although a strict detection threshold was employed, there are false detections that are
 165 caused by other signals, such as local or regional regular earthquakes or teleseismic events. To
 166 exclude local or regional earthquakes, we compared the origin time of detected events with a
 167 catalog of local and regional regular earthquakes constructed by El Observatorio Vulcanológico y
 168 Sismológico de Costa Rica, Universidad Nacional (Catálogo de Temblores de Costa Rica, 2004-
 169 2006; Protti, personal comm.). We discarded events whose epicentral distances were less than 150
 170 km and origin times were within ± 50 s from the local or regional earthquakes listed in this
 171 earthquake catalog. To discard false detections by teleseismic events, we removed the events
 172 detected between the P -wave arrivals and 600 s after S -wave arrivals of teleseismic events ($M_w \geq$
 173 5) in the catalog of the United States Geological Survey. The event amplitudes and CCs are
 174 positively correlated in general, but events with high amplitudes and low average CCs occasionally
 175 appear. These events are considered to be false detections due to teleseismic events absent in the
 176 catalogs. Therefore, we did not count events with average CCs below 0.56 and relative amplitudes
 177 to templates higher than 0.4 (Baba et al., 2018; 2020a). If the amplitude relative to the template
 178 with M_w of 4.0 was smaller than 0.05, we did not count the event because the signal was too small
 179 to judge whether the event is truly existed or not.

180 For the remaining events, we calculated the variance reduction (VR) between the template
 181 and observed waveforms. We estimated VRs using only the vertical component seismograms of
 182 relatively quiet stations in and around the Nicoya Peninsula (MANS, CABA, FINA, CRUP, and
 183 PALM), because differences of amplitude distributions between updip and downdip events are
 184 large in these stations:

$$185 \quad VR = \left[1 - \frac{\sum_i \int \{f_i(t) - cg_i(t)\}^2 dt}{\sum_i \int \{f_i(t)\}^2 dt} \right] \times 100\% , \quad (1)$$

186 where $f_i(t)$ and $g_i(t)$ are the observed and template waveforms at the i -th station, respectively,
 187 and c is the relative amplitude of the observed waveform to the template. We selected events whose
 188 VRs were larger than 30%. This threshold is set by trial and error based on visual identifications
 189 of VLFEs in the observed data.

190 After the above procedures, falsely detected events still remained because we only used the
 191 vertical component seismograms, and the array configuration was cross shaped. To discard the
 192 remaining false detections, we estimated the normalized-and-stacked amplitude, azimuth, and

193 velocity of signal propagation by applying delay-and-sum beamforming (Section 3.1 of Rost &
 194 Thomas, 2002; Walter et al., 2013) to vertical component seismograms. After normalizing the
 195 waveform of each station by its maximum amplitude in the 150 s time window, we searched for
 196 the azimuth and velocity that maximized the stacked amplitude by performing a grid search for
 197 the azimuth between $135^\circ - 315^\circ$ with 1° intervals and the velocity between 2–5 km/s with 0.1
 198 km/s intervals. We first used the along-strike stations in both Costa Rica and Nicaragua (brown
 199 inverted triangles in Figure 1b) to discard teleseismic events. The amplitudes of Costa Rican
 200 VLFs at the Nicaraguan stations are generally very small compared with those in the Costa Rican
 201 stations due to geometrical spreading, but amplitudes for teleseismic events are similar. Therefore,
 202 we selected events whose stacked normalized amplitude normalized by the number of stations was
 203 smaller than 0.6 because events with large stacked signals are suspected to be teleseismic
 204 earthquakes (Figure S4). We then conducted another beamforming analysis for the remaining
 205 events using the same stations as the matched-filter analysis, and selected events whose azimuth
 206 was $200-230^\circ$. Finally, to avoid duplicate detection, only one event was counted every 60 s from
 207 the remaining VLFE candidates. We only counted the event whose averaged CC was the highest
 208 spatiotemporally.

209 **2.1.4. Estimation of the moments of events**

210 We estimated the source durations of detected VLFs by comparing template waveforms
 211 with source durations of 10–50 s and an M_w of 4.0 with observed waveforms (e.g., Yabe et al.,
 212 2021). The source duration that resulted in the highest values of CC between the observed and
 213 template waveforms was adopted.

214 We also calculated the amplitude of an event relative to the template waveforms using the
 215 same method as Baba et al. (2020b). The relative amplitude can be used to calculate the seismic
 216 moment of each VLFE. The seismic moment rate of a VLFE was calculated by dividing its seismic
 217 moment by its source duration. To evaluate the estimation error of moment rates of VLFs, we
 218 calculated moment rates by assuming the various source durations whose CCs between synthetic
 219 and observed waveforms are more than 90% of the maximum CC. Although there are errors in the
 220 order of 0.2, we verified that the order of moment rates does not change (Figure S5).

221 **2.2. Results**

222 We detected 68 VLFs during the analysis period. Example traces of a VLFE located at
 223 85.8°W and 9.4°N are shown in Figure 3. The signal of this VLFE first arrives at MANS and
 224 propagates to inland stations (top panel of Figure 3). This feature was successfully modeled for
 225 the updip templates (Fig. 2b). There is a tremor signal in the frequency range of 2–8 Hz in the
 226 same time window (middle and bottom panels of Figure 3). The cumulative number of VLFs
 227 showed significant increases in September 2004 and August 2005 (Figure 4a). In August 2005, an
 228 SSE was reported by Jiang et al. (2012); therefore, SSE and VLFE activities were temporally
 229 correlated. The M_w and source duration of VLFs were mainly distributed in 3.4–4.2 and 10–30
 230 s, respectively (Figures 5a, b). The M_w and source duration of VLFs have a positive correlation
 231 (Figure 5c) like shallow VLFs in Nankai, Japan (Sugioka et al., 2012; Takemura et al., 2019).

232 Most of the VLFs (62 events) are distributed where the plate boundary is at a depth range
 233 of 6–10 km below the sea level, near the trench axis off the Nicoya Peninsula (Figure 4b), at the
 234 updip of the seismogenic zone. The distribution of these VLFs is consistent with the VLFs in
 235 2008 suggested by Walter et al. (2013). When locating some events using both vertical and
 236 horizontal component seismograms whose signal to noise (SN) ratios are relatively high for the

237 verification of the analysis by using vertical components only, the high CC areas overlap and the
238 epicenters were also located near the trench axis, although there are differences of $0.1\text{--}0.2^\circ$ (Figure
239 S2). The area overlaps with the shallower part of the large slip area of the 2007 SSE (Jiang et al.,
240 2017) or summed SSE slip in 2007–2012 (Dixon et al., 2014). Although the slip distribution of the
241 2005 SSE was not estimated in previous studies, our results suggest that the 2005 SSE can also
242 have a large slip area near the trench axis, similar to the 2007 SSE. The distribution of VLFs lies
243 within the gap between large slip areas of thrust-type large interplate earthquakes with an M_w of
244 7–8 around the Nicoya Peninsula and the 1992 tsunami earthquake with an M_w of 7.6. The
245 distribution of VLFs also separated from the afterslip area of the 2012 M_w 7.6 earthquake
246 (Malservisi et al., 2015).

247 The distribution of the CC shows the resolution of the location of VLFs. By the
248 distribution of CC, it is confirmed that most of the VLFs were located near the trench axis. CCs
249 for more than half of the events exceeded the threshold only for updip templates (Figure 6a). For
250 several events, CCs exceeded the threshold both updip and downdip of the seismogenic zone with
251 a larger CC in the updip region. The area where CCs are more than 90% of the maximum CC is
252 concentrated only in the updip area (Figure 6b). On the other hand, 6 VLFs were located at a
253 depth of ~ 40 km at the downdip of large earthquakes (Figure 4b). Although focal mechanisms may
254 not be thrust-type and the areas where CCs are larger than the threshold are widely distributed, we
255 verified that regular earthquakes listed in the earthquake catalog by El Observatorio Vulcanológico
256 y Sismológico de Costa Rica in the updip and downdip areas are located in the updip and downdip
257 areas respectively by this method (Figure S6). However, we cannot exclude the possibility that
258 such VLFs occur in the updip region in real because, in such cases, two CC peaks tend to appear
259 both in the updip and downdip (Figure 6c). Of course, there is a possibility that such VLFs really
260 occur in the downdip region because the locations of such VLFs were near the locations of
261 previously reported LFs (Brown et al. 2009) and tremors (Outerbridge et al. 2010). In this study,
262 the SN ratios of VLFs detected in the downdip region are very low; hence, it is difficult to judge
263 whether such VLFs occur in downdip or updip, because it is hard to judge which station the
264 signal of the VLF arrival first due to the similar arrival times at updip stations. The reason for
265 the small number and the low SN ratio of downdip events may be that slow earthquakes in the
266 downdip region were inactive during 1.5 years of the temporary array. To investigate whether deep
267 VLFs really exist, an analysis with a longer dataset is needed in future work.

268 **3. Estimations of seismic energy rates for tremors accompanied by VLFs**

269 **3.1. Data and method**

270 Tremor signals were also found in the frequency range of 2–8 Hz within the time windows
271 of detected VLFs (middle panel of Figure 3; Figure S7). It is difficult to locate tremors in the
272 offshore region by using an onshore network because sources of tremors are distant from the
273 network and signals of tremors attenuate strongly compared to VLF (0.02–0.05 Hz) signals.
274 Based on the spatiotemporal correlation between VLFs and tremors reported in other regions
275 (e.g., Ghosh et al., 2015; Maeda & Obara, 2009; Tamaribuchi et al., 2019) and the interpretation
276 that VLFs and tremors are components of broadband slow earthquake phenomena (Gomberg et
277 al., 2016; Hawthorne & Bartlow, 2018; Ide & Maury, 2018), we estimated the energy rate functions
278 of tremors accompanied by VLFs by assuming that a tremor occurs at the same location as the
279 VLF (e.g., Yabe et al., 2019; 2021). We simulated the waveforms at the location of a VLF using
280 the same model which is described in Section 2.1.2 but discretized by a finer grid interval (0.04
281 km). The simulated envelope shapes are different from observed ones due to a simple pulse source

282 time function (details in the caption of Figure S8), but the arrival times of maximum *S*-wave
 283 amplitudes in the frequency range of 2–8 Hz are consistent with observed tremor waveforms
 284 (Figure S8). Therefore, we supposed that a VLFE and the corresponding tremor occurred at the
 285 same location.

286 We also used waveforms of the TUCAN network similarly to the VLFE detection. After
 287 applying a bandpass filter of 2–8 Hz, the envelope waveforms were calculated by taking the root-
 288 mean-square of sums of three-component squared seismograms and a smoothing time window of
 289 3 s (bottom panel of Figure 3). The envelope waveforms were resampled at one sample per second.

290 3.1.1. Quality factor of the apparent *S*-wave attenuation

291 To estimate the energy rate functions of tremors accurately, we estimated the quality factor
 292 of the apparent *S*-wave attenuation (Q_{app}), based on the coda-normalization method (e.g., Aki,
 293 1980; Yoshimoto et al., 1993). First, we selected some isolated regular earthquakes (Figure S9).
 294 To eliminate the effect of differences in source size and site amplification, observed maximum *S*-
 295 wave amplitudes were normalized by averaged coda amplitudes within a lapse time of 80–90 s.
 296 The coda-normalized maximum *S*-wave amplitude of the *i*-th earthquake at the *j*-th station (A_{ij})
 297 and the distance between the hypocenter of the *i*-th earthquake and *j*-th station (L_{ij}) have the
 298 following relationship (Takemura et al., 2017):

$$299 \ln(L_{ij}A_{ij}) = -\frac{\pi f_c Q_{app}^{-1}}{V_s} L_{ij} + C', \quad (2)$$

300 where V_s is the *S*-wave velocity (assuming 3.5 km/s in this study; Maeda & Obara, 2009; Yabe et
 301 al., 2019; 2021), f_c is the central frequency (assuming 5 Hz in this study), and C' is a constant. By
 302 solving Equation (2) by the least-squares method, we estimated Q_{app}^{-1} as $10^{-2.42}$ (Figure 7a).

303 3.1.2. Site amplification factor

304 We estimated the site amplification factor at 2–8 Hz using relative coda amplitudes (e.g.,
 305 Maeda and Obara, 2009). Coda amplitudes at a certain time window generally depend on the
 306 source size and site amplification (e.g., Chapters 2 and 3 of Sato et al., 2012). Therefore, the ratio
 307 of the coda wave amplitude at a station to that at a reference station for the same event depends
 308 only on the site amplification factor relative to a reference station.

309 We calculated the ratios of the coda amplitudes for each station to those of MANS
 310 (reference station) for each regular earthquake used in Section 3.1. The time window for evaluating
 311 relative coda amplitudes is the same as that in coda-normalization in Section 3.1. Then we
 312 calculated the average of the coda amplitude ratios of all earthquakes for each station. The
 313 estimated relative site amplification factors at each station used in the estimations of the energy
 314 rate functions of tremors are shown in Figure 7b. We compared coda amplitudes of regular
 315 earthquakes at MANS with those at the JTS, a permanent station of the Global Seismograph
 316 Network by Incorporated Research Institutions for Seismology and International Deployment of
 317 Accelerometers (Scripps Institution of Oceanography, 1986). The average ratio of coda amplitudes
 318 at MANS to those at JTS is 1.14, suggesting that the condition of MANS site is very similar to that
 319 of the JTS.

320 3.1.3. Seismic energy rate of tremors

321 By using apparent attenuation (Q_{app}^{-1}) and site amplification in the previous subsections,
 322 we estimated the energy rate functions of tremors. The source energy rate function of a tremor

323 ($E_j(t)$) using the amplitude of the j -th station is calculated by the following formula (Maeda &
324 Obara, 2009):

$$325 \quad E_j(t) = 2\pi V_S r_j^2 \rho A_j'^2(t + t_j) \exp(2\pi f_c Q_{app}^{-1} t_j), \quad (3)$$

326 where $A_j'(t)$ is the site-corrected amplitude of the envelope waveform of the j -th station, r_j is the
327 hypocentral distance from the accompanying VLFE, t_j is the travel time from the VLFE source,
328 and ρ is the density (assuming 2,700 kg/m³). For calculating $E_j(t)$, we used a 180 s time window
329 that started 60 s before the origin time of VLFES. We calculated the CCs of all station pairs in
330 Figure 7b. To estimate the source energy rate function of the tremor, we only used stations whose
331 CCs with at least one other station exceeded 0.6.

332 The seismic energy rate W_j using the amplitude of the j -th station is given by the integration
333 of the source energy rate function $E_j(t)$ in time:

$$334 \quad W_j = \frac{1}{t_2 - t_1} \int_{t_1}^{t_2} E_j(t) dt, \quad (4)$$

335 where t_1 and t_2 are the start and end of the integration range, respectively. The integration range is
336 defined as the period in which the values of $E_j(t)$ exceeded 20% of the maximum value of $E_j(t)$
337 (Figure 8). The seismic energy rate of a tremor (W_0) was obtained by calculating the average W_j
338 of all stations. The error of W_0 was obtained by calculating the standard deviation of W_j .

339 **3.2. Results**

340 The energy rates of tremors were mainly distributed in 10^3 – $10^{5.5}$ J/s (Figure 9). There is a
341 positive correlation between the energy rates of tremors and the moment rates of the corresponding
342 VLFES. We estimated the scaled energy by calculating the ratio between the seismic energy rate
343 of a tremor and the seismic moment rate of the corresponding VLFE. The scaled energy of slow
344 earthquakes off Costa Rica is mainly distributed in the range of 10^{-9} – 10^{-8} (dotted lines in Figure
345 9).

346 **4. Discussion**

347 **4.1. shallow ETS off Costa Rica**

348 The activation of VLFES and tremors in August 2005 temporally correlates with the 2005
349 SSE reported by Jiang et al. (2012). VLFES and tremors occurred mainly in the updip area in
350 August 2005; hence, the slip area of the 2005 SSE can be distributed in the updip area near the
351 trench axis, similar to the 2007 SSE. In areas where shallow VLFES occurred, subseafloor
352 hydrological observatories recorded pore fluid pressure transients in 2000 (Brown et al., 2005),
353 2003–2004 (Solomon et al., 2009), and 2007–2013 (Davis et al., 2011; 2015). They interpreted
354 that pore fluid pressure transients were caused by SSEs. Spatial correspondence of pore fluid
355 change in the periods of previous studies and VLFE activity in 2005 near the trench off Costa Rica
356 suggests the occurrence of a shallow ETS, as with the Nankai subduction zone (Araki et al., 2017;
357 Nakano et al., 2018).

358 **4.2. Separation of slow earthquakes and other phenomena**

359 Before the 2012 M_w 7.6 earthquake, the interplate coupling of the shallow slow earthquake
360 area at a plate-boundary depth range of 6–10 km was expected to be very weak (Feng et al., 2012)
361 unlike the coseismic slip area, which was strongly coupled (Protti et al., 2014). The average stress
362 drop of small-to-moderate regular earthquakes inside the large slip area of the 1992 tsunami

363 earthquake (surrounded by dark blue lines in Figure 4) was 1.2 MPa, which was smaller than that
364 outside the large slip area (Bilek et al., 2016). The values of reported stress drops of slow
365 earthquakes in the Nankai subduction zone were 0.1–200 kPa (e.g., Ito & Obara, 2006; Takagi et
366 al., 2019); therefore, we consider that the stress drops of slow earthquake area are also much
367 smaller than those of regular and tsunami earthquakes. The spatial variation of interplate coupling
368 and stress drop of slip at the plate boundary results from the heterogeneous distribution of frictional
369 properties at the plate boundary in the Central American subduction zone. In addition, a low stress
370 drop suggests a high pore pressure generated by the existence of fluids (Yao & Yang, 2020).
371 Therefore, the frictional strength of the slow earthquake area at a depth range of 6–10 km can be
372 quite weak owing to the rich fluid compared to that in the regions with regular and tsunami
373 earthquakes.

374 In Costa Rica, repeating earthquakes were activated after the 2012 M_w 7.6 earthquake
375 around the large coseismic slip area of the earthquake (Chaves et al., 2020). Such activation after
376 a large earthquake in the afterslip area was also observed in the Tohoku subduction zone (Uchida
377 & Matsuzawa, 2013). The locations of repeating earthquakes separate from the areas where VLFs
378 occur. Such separation is also found in the Nankai (e.g., Takemura et al., 2020) and the Tohoku
379 subduction zone (e.g., Nishikawa et al., 2019).

380 **4.3. Comparison with other subduction zones**

381 Our study revealed that shallow VLFs and tremors occur near the trench axis off Costa
382 Rica, in the updip of coseismic slip areas of thrust-type large earthquakes with an M_w of 7–8. In
383 the updip area, SSEs also occurred in 2007–2012 (Dixon et al., 2017; Jiang et al., 2012). The depth
384 range and the separate distribution between shallow slow earthquakes and large earthquakes off
385 Costa Rica are similar to shallow slow earthquakes in the Nankai subduction zone, where slow
386 earthquakes are spatially separated from high slip-deficit zones (e.g., Takemura et al., 2020). On
387 the other hand, before the 2011 Tohoku earthquake, shallow slow slip events propagated to the
388 initial rupture point of the great earthquake (Kato et al., 2012). Therefore, the characteristics of
389 distribution of slow and large earthquakes differ between Tohoku and Costa Rica.

390 There are other common features in shallow slow earthquakes between Costa Rica and
391 Nankai. Although the lower limit of M_w is large (~ 3.4) due to a strict threshold, the ranges of
392 magnitudes and source durations of shallow VLFs off Costa Rica are similar to those of shallow
393 VLFs in the Nankai subduction zones (e.g., Takemura et al., 2019). The recurrence intervals of
394 activation of slow earthquakes are one to several years in Costa Rica (Jiang et al., 2012), which is
395 similar to shallow slow earthquakes in the Nankai subduction zone, but different from the shorter
396 intervals of deep slow earthquakes in Nankai (e.g., Baba et al., 2020b). Although the number of
397 tremors whose energy rates are less than 10^4 J/s is small because of the strict detection threshold
398 of the corresponding VLFs, the upper limit of the energy rate range of tremors is similar to that
399 observed for shallow tremors in Nankai (Yabe et al., 2019). The estimated scaled energy of slow
400 earthquakes off Costa Rica is also similar to that of shallow slow earthquakes in the Nankai
401 subduction zone (Yabe et al., 2019). The scaled energy is related to the rupture process of seismic
402 phenomena (Kanamori & Rivera, 2006), therefore these results suggest that the frictional
403 properties within the shallow slow earthquake areas are similar in both Costa Rica and Nankai. On
404 the other hand, the scaled energy range in both regions is 0.5–1 orders of magnitude larger than
405 that of shallow slow earthquakes in the Tohoku subduction zone (Yabe et al., 2021), and
406 approximately 1 order of magnitude larger than that of deep slow earthquakes in Nankai (Ide et
407 al., 2008; Ide & Yabe, 2014; Ide, 2016; Ide & Maury, 2018; Maeda & Obara, 2009). We note that

408 scaled energies of shallow slow earthquakes were estimated for individual events, whereas those
409 of deep slow earthquakes estimated by Ide & Yabe (2014), Ide (2016), and Ide & Maury (2018)
410 were estimated for stacked events.

411 The range of scaled energy and distribution of shallow slow earthquakes off Costa Rica are
412 more similar to those in shallow Nankai than shallow Tohoku. According to Syracuse et al. (2010),
413 the age and thermal parameters of Costa Rica are 15.8 Ma and 1,010 km, respectively, which are
414 closer to those of Nankai (20.0 Ma and 450 km, respectively) than Tohoku (115.2–130.5 Ma and
415 5,720–6,040 km, respectively). The thermal parameter, which is product of the incoming plate age,
416 the convergence rate, and the sine of the slab dip angle, is used to predict the slab surface
417 temperature at a given depth (e.g., Kirby et al., 1991; Syracuse et al., 2010). In addition, the
418 temperatures of shallower parts of plate interfaces of these subduction zones where shallow slow
419 earthquakes are not so different (Nankai: ~ 100 °C in the depth range of 0–5 km from the seafloor;
420 Tohoku: 65–110 °C in the depth range of 6–12 km; and Costa Rica: 12–60°C in the depth range of
421 0–10 km; Saffer & Wallace, 2015). On the other hand, the Central American subduction zone is
422 subduction of fast convergence rate (~ 8 cm/year; DeMets et al., 1994), high dip angle, and
423 erosional type (e.g., Bangs et al., 2016), which are more similar to Tohoku than Nankai. Although
424 the characteristics of slow earthquake activity can be related to various factors, the thermal
425 parameter and incoming plate age of Costa Rica is more similar to Nankai than Tohoku. The
426 temperature structure of the shallow plate interface is probably most sensitive to incoming plate
427 age (Maunder et al., 2019) and secondarily to thermal parameter (Syracuse et al., 2010). Hence,
428 similar temperature conditions on the interface may explain the common features of shallow slow
429 earthquakes off Costa Rica and in Nankai.

430 In previous studies, the large slip area of the SSE in 2007 was separated into deeper and
431 shallower parts (Jiang et al., 2017), and deep LFEs and tremors were detected downdip of the
432 seismogenic zone (Brown et al., 2009; Outerbridge et al., 2010). And, several VLFs were located
433 in the downdip area, in the similar area reported in previous studies of tremors and LFEs. If these
434 deep VLFs, LFEs and tremors occur in the downdip area, slow earthquakes might occur at
435 separate depths along both shallower and deeper extensions of rupture zones of large earthquakes
436 (Figure 10). This characteristic might also be the same as that of the Nankai subduction zone
437 (Obara & Kato, 2016). This suggests that the tectonic property may be similar in the wide depth
438 range in Costa Rica and Nankai. On the other hand, slow earthquakes are distributed only in the
439 deeper part in the Cascadia subduction zone and only in the shallower part in the Tohoku
440 subduction zone. The variation of the distribution of slow earthquakes may be attributed to the
441 difference in tectonics or detection capability. The elucidation of the reason for the difference of
442 the distribution in slow earthquake is future works.

443 5. Conclusions

444 Based on the grid-search matched-filter technique using synthetic templates in the regional
445 3D model, we detected and located VLFs around the Nicoya Peninsula. Many VLFs occurred
446 in September 2004 and August 2005, and more than 90% of the VLFs were located near the
447 trench axis, where the plate boundary is at a depth range of 6–10 km, updip of the seismogenic
448 zone, whereas several VLFs were located in the downdip area at a depth of ~ 40 km. In this area,
449 the occurrence of shallow SSEs is suggested by VLFE episodes. The region with VLFE activity
450 overlaps with the shallower part of the large slip area of the 2007 SSE; therefore, the occurrences
451 of shallow SSEs are suggested in September 2004 and August 2005 to occur in the same area as
452 the shallower part of the 2007 SSE. The distribution of VLFs lies in the gap surrounding

453 coseismic slip areas of tsunami and large regular earthquakes. This separation reflects the spatial
 454 distribution of the frictional strength of the plate boundary in the Central American subduction
 455 zone. By using high-frequency seismogram envelopes, we also estimated the energy rates of
 456 tremors accompanying VLFs. The ranges of magnitude and source duration of VLFs, energy
 457 rate of tremors, and scaled energy off Costa Rica are similar to those in shallow slow earthquakes
 458 in the Nankai subduction zone.

459 **Data Availability**

460 We used seismograms of the TUCAN network (Abers & Fischer, 2003;
 461 https://doi.org/10.7914/SN/YO_2003) and Global Seismograph Network (Scripps Institution of
 462 Oceanography, 1986; <https://doi.org/10.7914/SN/II>). We used the earthquake catalog of the U.S.
 463 Geological Survey (<https://earthquake.usgs.gov/earthquakes/search/>). We used OpenSWPC code
 464 Version 5.0.2 (Maeda et al., 2017; <https://doi.org/10.5281/zenodo.3712650>) for the numerical
 465 simulations. Numerical simulations were conducted using the Fujitsu PRIMERGY
 466 CX600M1/CX1640M1 (Oakforest-PACS) at the Information Technology Center, the University
 467 of Tokyo. We used generic mapping tools (Wessel et al., 2013) and Seismic Analysis Code
 468 (Helfrich et al., 2013) to prepare the figures and process seismograms, respectively. The VLF
 469 and tremor catalog constructed by this study is provided in an open access repository, zenodo (doi:
 470 [10.5281/zenodo.4435232](https://doi.org/10.5281/zenodo.4435232)).

471 **Acknowledgements**

472 We would like to thank the editor, the associate editor and the two anonymous reviewers
 473 for their valuable comments and suggestions. We would like to thank Suguru Yabe for valuable
 474 discussions. We would also like to thank Marino Protti for providing the earthquake catalog in
 475 Costa Rica and for discussions. We thank Editage (www.editage.com) for English proofreading.
 476 This research was supported by JSPS KAKENHI Grant in Science Research on Innovative Areas
 477 “Science of Slow Earthquakes” (JP16H06473) and JSPS Research Fellowship DC1 (JP19J20760).
 478 This study was also supported by the ERI-JURP 2020-S-04.

479 **References**

- 480 Abers, G. A., & Fischer, K. M. (2003). Tomography Under Costa Rica and Nicaragua.
 481 International Federation of Digital Seismograph Networks.
 482 https://doi.org/10.7914/SN/YO_2003
- 483 Aki, K. (1980). Attenuation of shear-waves in the lithosphere for frequencies from 0.05 to 25 Hz.
 484 *Physics of the Earth and Planetary Interiors*, 21(1), 50–60. [https://doi.org/10.1016/0031-](https://doi.org/10.1016/0031-9201(80)90019-9)
 485 [9201\(80\)90019-9](https://doi.org/10.1016/0031-9201(80)90019-9)
- 486 Amante, C., & Eakins, B.W. (2009). ETOPO1 1 Arc-Minute Global Relief Model: Procedures,
 487 Data Sources and Analysis. NOAA Technical Memorandum NESDIS NGDC-24.
 488 <https://doi.org/10.7289/V5C8276M>
- 489 Araki, E., Saffer, D. M., Kopf, A. J., Wallace, L. M., Kimura, T., Machida, Y., et al. (2017).
 490 Recurring and triggered slow-slip events near the trench at the Nankai Trough subduction
 491 megathrust. *Science*, 356(6343), 1157–1160. <https://doi.org/10.1126/science.aan3120>
- 492 Baba, S., Takeo, A., Obara, K., Kato, A., Maeda, T., & Matsuzawa, T. (2018). Temporal
 493 Activity Modulation of Deep Very Low Frequency Earthquakes in Shikoku, Southwest
 494 Japan. *Geophysical Research Letters*, 45(2), 733–738.
 495 <https://doi.org/10.1002/2017GL076122>

- 496 Baba, S., Takeo, A., Obara, K., Matsuzawa, T., & Maeda, T. (2020a). Comprehensive Detection
 497 of Very Low Frequency Earthquakes Off the Hokkaido and Tohoku Pacific Coasts,
 498 Northeastern Japan. *Journal of Geophysical Research: Solid Earth*, *125*(1), 1–13.
 499 <https://doi.org/10.1029/2019JB017988>
- 500 Baba, S., Takemura, S., Obara, K., & Noda, A. (2020b). Slow Earthquakes Illuminating
 501 Interplate Coupling Heterogeneities in Subduction Zones. *Geophysical Research Letters*,
 502 *47*(14), 4–5. <https://doi.org/10.1029/2020GL088089>
- 503 Bangs, N. L., McIntosh, K. D., Silver, E. A., Kluesner, J. W., & Ranero, C. R. (2016). A recent
 504 phase of accretion along the southern Costa Rican subduction zone. *Earth and Planetary
 505 Science Letters*, *443*, 204–215. <https://doi.org/10.1016/j.epsl.2016.03.008>
- 506 Bilek, S. L., Rotman, H. M. M., & Phillips, W. S. (2016). Low stress drop earthquakes in the
 507 rupture zone of the 1992 Nicaragua tsunami earthquake. *Geophysical Research Letters*,
 508 *43*(19), 10,180–10,188. <https://doi.org/10.1002/2016GL070409>
- 509 Brown, J. R., Beroza, G. C., Ide, S., Ohta, K., Shelly, D. R., Schwartz, S. Y., et al. (2009). Deep
 510 low-frequency earthquakes in tremor localize to the plate interface in multiple subduction
 511 zones. *Geophysical Research Letters*, *36*(19), 1–5. <https://doi.org/10.1029/2009GL040027>
- 512 Brown, K. M., Tryon, M. D., DeShon, H. R., Dorman, L. R. M., & Schwartz, S. Y. (2005).
 513 Correlated transient fluid pulsing and seismic tremor in the Costa Rica subduction zone.
 514 *Earth and Planetary Science Letters*, *238*(1–2), 189–203.
 515 <https://doi.org/10.1016/j.epsl.2005.06.055>
- 516 Chaves, E. J., Schwartz, S. Y., & Abercrombie, R. E. (2020). Repeating earthquakes record fault
 517 weakening and healing in areas of megathrust postseismic slip, 2–10.
- 518 Christensen, N. I., & Salisbury, M. H. (1975). Structure and constitution of the lower oceanic
 519 crust. *Reviews of Geophysics*, *13*(1), 57–86. <https://doi.org/10.1029/RG013i001p00057>
- 520 Davis, E., Heesemann, M., & Wang, K. (2011). Evidence for episodic aseismic slip across the
 521 subduction seismogenic zone off Costa Rica: CORK borehole pressure observations at the
 522 subduction prism toe. *Earth and Planetary Science Letters*, *306*(3–4), 299–305.
 523 <https://doi.org/10.1016/j.epsl.2011.04.017>
- 524 Davis, E. E., Villinger, H., & Sun, T. (2015). Slow and delayed deformation and uplift of the
 525 outermost subduction prism following ETS and seismogenic slip events beneath Nicoya
 526 Peninsula, Costa Rica. *Earth and Planetary Science Letters*, *410*, 117–127.
 527 <https://doi.org/10.1016/j.epsl.2014.11.015>
- 528 DeMets, C., Gordon, R. G., Argus, D. F., & Stein, S. (1994). Effect of recent revisions to the
 529 geomagnetic reversal time scale on estimates of current plate motions. *Geophysical
 530 Research Letters*, *21*(20), 2191–2194. <https://doi.org/10.1029/94GL02118>
- 531 Dixon, T. H., Jiang, Y., Malservisi, R., McCaffrey, R., Voss, N., Protti, M., & Gonzalez, V.
 532 (2014). Earthquake and tsunami forecasts: Relation of slow slip events to subsequent
 533 earthquake rupture. *Proceedings of the National Academy of Sciences of the United States
 534 of America*, *111*(48), 17039–17044. <https://doi.org/10.1073/pnas.1412299111>
- 535 Dragert, H., Wang, K., James, T. S. (2001). A Silent Slip Event on the Deeper Cascadia
 536 Subduction Interface. *Science*, *292*(5521), 1525–1528.
 537 <https://doi.org/10.1126/science.1060152>
- 538 Feng, L., Newman, A. V., Protti, M., Gonzalez, V., Jiang, Y., & Dixon, T. H. (2012). Active
 539 deformation near the Nicoya Peninsula, northwestern Costa Rica, between 1996 and 2010:
 540 Interseismic megathrust coupling. *Journal of Geophysical Research: Solid Earth*, *117*(6),
 541 1–23. <https://doi.org/10.1029/2012JB009230>

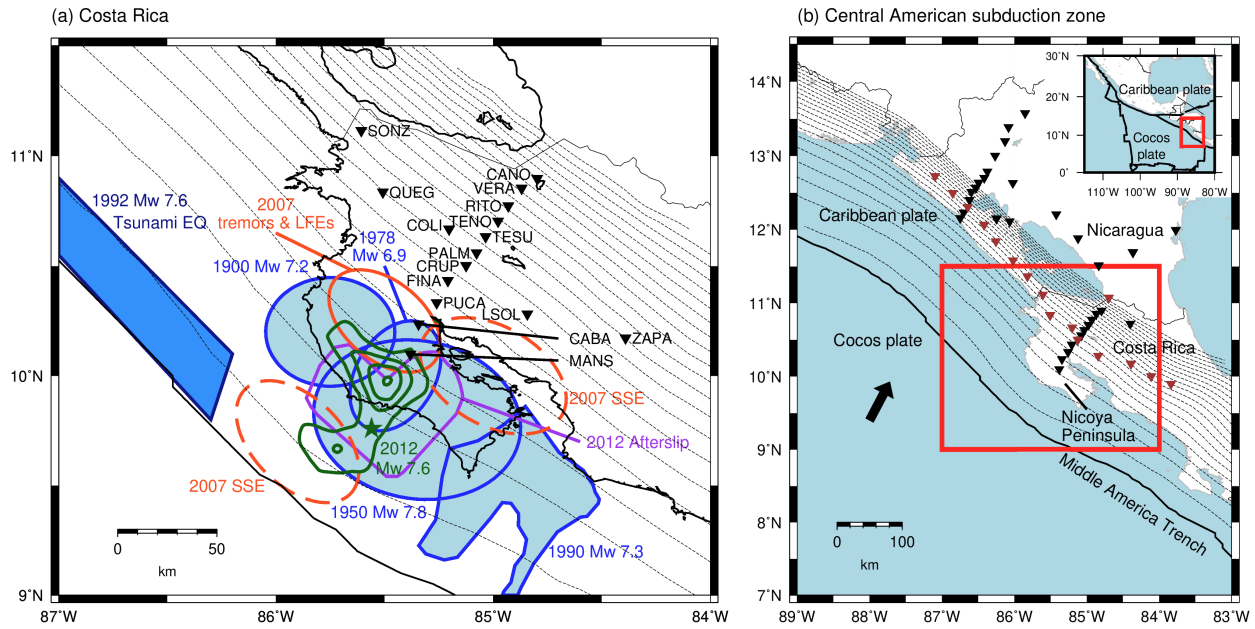
- 542 Ghosh, A., Huesca-Pérez, E., Brodsky, E., & Ito, Y. (2015). Very low frequency earthquakes in
543 Cascadia migrate with tremor. *Geophysical Research Letters*, *42*(9), 3228–3232.
544 <https://doi.org/10.1002/2015GL063286>
- 545 Gomberg, J., Wech, A., Creager, K., Obara, K., & Agnew, D. (2016). Reconsidering earthquake
546 scaling. *Geophysical Research Letters*, *43*(12), 6243–6251.
547 <https://doi.org/10.1002/2016GL069967>
- 548 Hasselmann, K. (1963). A statistical analysis of the generation of microseisms. *Reviews of*
549 *Geophysics*, *1*, 177–209. <https://doi.org/10.1029/RG001i002p00177>
- 550 Hawthorne, J. C., & Bartlow, N. M. (2018). Observing and Modeling the Spectrum of a Slow
551 Slip Event. *Journal of Geophysical Research: Solid Earth*, *123*(5), 4243–4265.
552 <https://doi.org/10.1029/2017JB015124>
- 553 Hayes, G. P., Moore, G. L., Portner, D. E., Hearne, M., Flamme, H., Furtney, M., & Smoczyk,
554 G. M. (2018). Slab2, a Comprehensive Subduction Zone Geometry Model, *Science*,
555 *61*(October), 58–61. <https://doi.org/10.1126/science.aat4723>
- 556 Helffrich, G., Wookey, J., & Bastow, I. (2013). The Seismic Analysis Code. Cambridge:
557 Cambridge University Press. <https://doi.org/10.1017/CBO9781139547260>
- 558 Hutchison, A. A. (2020). Interepisodic Tremor and Slip Event Episodes of Quasi-
559 spatiotemporally Discrete Tremor and Very Low Frequency Earthquakes in Cascadia
560 Suggestive of a Connective Underlying, Heterogeneous Process. *Geophysical Research*
561 *Letters*, *47*(3), 1–7. <https://doi.org/10.1029/2019GL086798>
- 562 Hutchison, A. A., & Ghosh, A. (2016). Very low frequency earthquakes spatiotemporally
563 asynchronous with strong tremor during the 2014 episodic tremor and slip event in
564 Cascadia. *Geophysical Research Letters*, *43*(13), 6876–6882.
565 <https://doi.org/10.1002/2016GL069750>
- 566 Hutchison, A. A., & Ghosh, A. (2019). Repeating VLFs During ETS Events in Cascadia Track
567 Slow Slip and Continue Throughout Inter-ETS Period. *Journal of Geophysical Research:*
568 *Solid Earth*, *124*(1), 554–565. <https://doi.org/10.1029/2018JB016138>
- 569 Ide, S. (2016). Characteristics of slow earthquakes in the very low frequency band: Application
570 to the Cascadia subduction zone. *Journal of Geophysical Research: Solid Earth*, *121*(8),
571 5942–5952. <https://doi.org/10.1002/2016JB013085>
- 572 Ide, S., & Maury, J. (2018). Seismic Moment, Seismic Energy, and Source Duration of Slow
573 Earthquakes: Application of Brownian slow earthquake model to three major subduction
574 zones. *Geophysical Research Letters*, *45*(7), 3059–3067.
575 <https://doi.org/10.1002/2018GL077461>
- 576 Ide, S., & Yabe, S. (2014). Universality of slow earthquakes in the very low frequency band.
577 *Geophysical Research Letters*, *41*(8), 2786–2793. <https://doi.org/10.1002/2014GL059712>
- 578 Ide, S., Imanishi, K., Yoshida, Y., Beroza, G. C., & Shelly, D. R. (2008). Bridging the gap
579 between seismically and geodetically detected slow earthquakes. *Geophysical Research*
580 *Letters*, *35*(10), 2–7. <https://doi.org/10.1029/2008GL034014>
- 581 Ito, Y., Obara, K., Shiomi, K., Sekine, S., & Hirose, H. (2007). Slow Earthquakes Coincident
582 with Episodic Tremors and Slow Slip Events. *Science*, *315*(5811), 503–506.
583 <https://doi.org/10.1126/science.1134454>
- 584 Ito, Y., & Obara, K. (2006). Very low frequency earthquakes within accretionary prisms are very
585 low stress-drop earthquakes. *Geophysical Research Letters*, *33*(9), 1–4.
586 <https://doi.org/10.1029/2006GL025883>

- 587 Ito, Y., Obara, K., Matsuzawa, T., & Maeda, T. (2009). Very low frequency earthquakes related
 588 to small asperities on the plate boundary interface at the locked to aseismic transition.
 589 *Journal of Geophysical Research: Solid Earth*, *114*(11), 1–16.
 590 <https://doi.org/10.1029/2008JB006036>
- 591 Ito, Y., Hino, R., Kido, M., Fujimoto, H., Osada, Y., Inazu, D., Ohta, Y., Inuma, T., Ohzono,
 592 M., Miura, S., Mishina, M., Suzuki, K., Tsuji, T., & Ashi, J. (2013). Episodic slow slip
 593 events in the Japan subduction zone before the 2011 Tohoku-Oki earthquake.
 594 *Tectonophysics*, *600*, 14–26. <https://doi.org/10.1016/j.tecto.2012.08.022>
- 595 Jiang, Y., Wdowinski, S., Dixon, T. H., Hackl, M., Protti, M., & Gonzalez, V. (2012). Slow slip
 596 events in Costa Rica detected by continuous GPS observations, 2002–2011. *Geochemistry,*
 597 *Geophysics, Geosystems*, *13*(1), 1–18. <https://doi.org/10.1029/2012GC004058>
- 598 Jiang, Y., Liu, Z., Davis, E. E., Schwartz, S. Y., Dixon, T. H., Voss, N., et al. (2017). Strain
 599 release at the trench during shallow slow slip: The example of Nicoya Peninsula, Costa
 600 Rica. *Geophysical Research Letters*, *44*(10), 4846–4854.
 601 <https://doi.org/10.1002/2017GL072803>
- 602 Kanamori, H., & Rivera, L. (2006). Energy partitioning during an earthquake. *Geophysical*
 603 *Monograph Series*, *170*, 3–13. <https://doi.org/10.1029/170GM03>
- 604 Kaneko, L., Ide, S., & Nakano, M. (2018). Slow Earthquakes in the Microseism Frequency Band
 605 (0.1–1.0 Hz) off Kii Peninsula, Japan. *Geophysical Research Letters*, *45*(6), 2618–2624.
 606 <https://doi.org/10.1002/2017GL076773>
- 607 Kato, A., & Nakagawa, S. (2014). Multiple slow-slip events during a foreshock sequence of the
 608 2014 Iquique, Chile Mw 8.1 earthquake. *Geophysical Research Letters*, *41*, 6413–6419.
 609 <https://doi.org/10.1002/2014GL061184>.
- 610 Kato, A., Obara, K., Igarashi, T., Tsuruoka, H., Nakagawa, S., & Hirata, N. (2012). Propagation
 611 of Slow Slip Leading Up to the 2011 Mw 9.0 Tohoku-Oki Earthquake. *Science*, *335*(6069),
 612 705–708. <https://doi.org/10.1126/science.1215141>
- 613 Kirby, S. T., Durham, W. B., & Stern, L. A. (1991). Mantle Phase Changes and Deep-
 614 Earthquake Faulting in Subducting Lithosphere. *Science*, *252*(5003), 216–225.
 615 <https://doi.org/10.1126/science.252.5003.216>
- 616 Laske, G., Masters, G., Ma, Z., & Pasyanos, M. (2013). Update on CRUST1.0 - A 1-degree
 617 Global Model of Earth's Crust, Paper presented at EGU General Assembly, European
 618 Geoscience Union, Vienna
- 619 Maeda, T., & Obara, K. (2009). Spatiotemporal distribution of seismic energy radiation from
 620 low-frequency tremor in western Shikoku, Japan. *Journal of Geophysical Research: Solid*
 621 *Earth*, *114*(10). <https://doi.org/10.1029/2008JB006043>
- 622 Maeda, T., Takemura, S., & Furumura, T. (2017). OpenSWPC: An open-source integrated
 623 parallel simulation code for modeling seismic wave propagation in 3D heterogeneous
 624 viscoelastic media 4. *Seismology. Earth, Planets and Space*, *69*(1).
 625 <https://doi.org/10.1186/s40623-017-0687-2>
- 626 Malservisi, R., Schwartz, S.Y., Voss, N., Protti, M., Gonzalez, V., Dixon, T.H., Jian, Y.,
 627 Newman, A.V., Walter, J.I., & Vayenko, D. (2015). Multiscale postseismic behavior on a
 628 megathrust: The 2012 Nicoya earthquake, Costa Rica. *Geochemistry, Geophysics,*
 629 *Geosystems*, *16*, 1848–1864. <https://doi.org/10.1002/2015GC005794>.
- 630 Maunder, B., van Hunen, J., Bouilhol, P., & Magni, V. (2019). Modeling Slab Temperature: A
 631 Reevaluation of the Thermal Parameter. *Geochemistry, Geophysics, Geosystems*, *20*(2),
 632 673–687. <https://doi.org/10.1029/2018GC007641>

- 633 Nadeau, R. M., & Dolenc, D. (2005). Nonvolcanic tremors deep beneath the San Andreas Fault.
634 *Science*, 307(5708), 389. <https://doi.org/10.1126/science.1107142>
- 635 Nakano, M., Hori, T., Araki, E., Kodaira, S., & Ide, S. (2018). Shallow very-low-frequency
636 earthquakes accompany slow slip events in the Nankai subduction zone /704/2151/210
637 /704/2151/508 article. *Nature Communications*, 9(1). [https://doi.org/10.1038/s41467-018-](https://doi.org/10.1038/s41467-018-03431-5)
638 03431-5
- 639 Nishikawa, T., Matsuzawa, T., Ohta, K., Uchida, N., Nishimura, T., & Ide, S. (2019). The slow
640 earthquake spectrum in the Japan Trench illuminated by the S-net seafloor observatories.
641 *Science (New York, N.Y.)*, 365(6455), 808–813. <https://doi.org/10.1126/science.aax5618>
- 642 Obara, K. (2002). Nonvolcanic Deep Tremor Associated with Subduction in Southwest Japan.
643 *Science*, 296(5573), 1679–1681. <https://doi.org/10.1126/science.1070378>
- 644 Obara, K. (2011). Characteristics and interactions between non-volcanic tremor and related slow
645 earthquakes in the Nankai subduction zone, southwest Japan. *Journal of Geodynamics*,
646 52(3–4), 229–248. <https://doi.org/10.1016/j.jog.2011.04.002>
- 647 Obara, K., & Ito, Y. (2005). Very low frequency earthquakes excited by the 2004 off Kii
648 peninsula earthquakes: A dynamic deformation process in the large accretionary prism.
649 *Earth, Planets and Space*, 57(4), 321–326. <https://doi.org/10.1186/BF03352570>
- 650 Obara, K., & Kato, A. (2016). Connecting slow earthquakes to huge earthquakes. *Science (New*
651 *York, N.Y.)*, 353(6296), 253–257. <https://doi.org/10.1126/science.aaf1512>
- 652 Outerbridge, K. C., Dixon, T. H., Schwartz, S. Y., Walter, J. I., Protti, M., Gonzalez, V., et al.
653 (2010). A tremor and slip event on the Cocos-Caribbean subduction zone as measured by a
654 global positioning system (GPS) and seismic network on the Nicoya Peninsula, Costa Rica.
655 *Journal of Geophysical Research: Solid Earth*, 115(10), 1–17.
656 <https://doi.org/10.1029/2009JB006845>
- 657 Protti, M. (1995). The March 25, 1990 (Mw=7.0, ML=6.8), earthquake at the entrance of the
658 Nicoya Gulf, Costa Rica: its prior activity, foreshocks, aftershocks, and triggered seismicity.
659 *Journal of Geophysical Research*, 100(B10), 345–358. <https://doi.org/10.1029/94jb03099>
- 660 Protti, M., González, V., Newman, A. V., Dixon, T. H., Schwartz, S. Y., Marshall, J. S., et al.
661 (2014). Nicoya earthquake rupture anticipated by geodetic measurement of the locked plate
662 interface. *Nature Geoscience*, 7(2), 117–121. <https://doi.org/10.1038/ngeo2038>
- 663 Rogers, G., & Dragert, H. (2003). Episodic Tremor and Slip on the Cascadia Subduction Zone:
664 The Chatter of Silent Slip. *Science*, 300(5627), 1942–1943.
665 <https://doi.org/10.1126/science.1084783>
- 666 Rost, S., & Thomas, C. (2002). Array seismology: Methods and applications. *Reviews of*
667 *Geophysics*, 40(3), 2-1-2–27. <https://doi.org/10.1029/2000RG000100>
- 668 Ruiz, S., Aden-Antoniow, F., Baez, J. C., Otarola, C., Potin, B., del Campo, F., et al. (2017).
669 Nucleation Phase and Dynamic Inversion of the M w 6.9 Valparaíso 2017 Earthquake in
670 Central Chile. *Geophysical Research Letters*, 44(20), 10,290-10,297.
671 <https://doi.org/10.1002/2017GL075675>
- 672 Saffer, D. M., & Wallace, L. M. (2015). The frictional, hydrologic, metamorphic and thermal
673 habitat of shallow slow earthquakes. *Nature Geoscience*, 8(8), 594–600.
674 <https://doi.org/10.1038/ngeo2490>
- 675 Satake, K. (1994). Mechanism of the 1992 Nicaragua Tsunami Earthquake. *Geophysical*
676 *Research Letters*, 21(23), 2519–2522. <https://doi.org/10.1029/94GL02338>
- 677 Sato, H., Fehler, M., & Maeda, T. (2012). Seismic Wave Propagation and Scattering in the
678 Heterogeneous Earth Structure, 2nd ed., New York, Springer-Verlag.

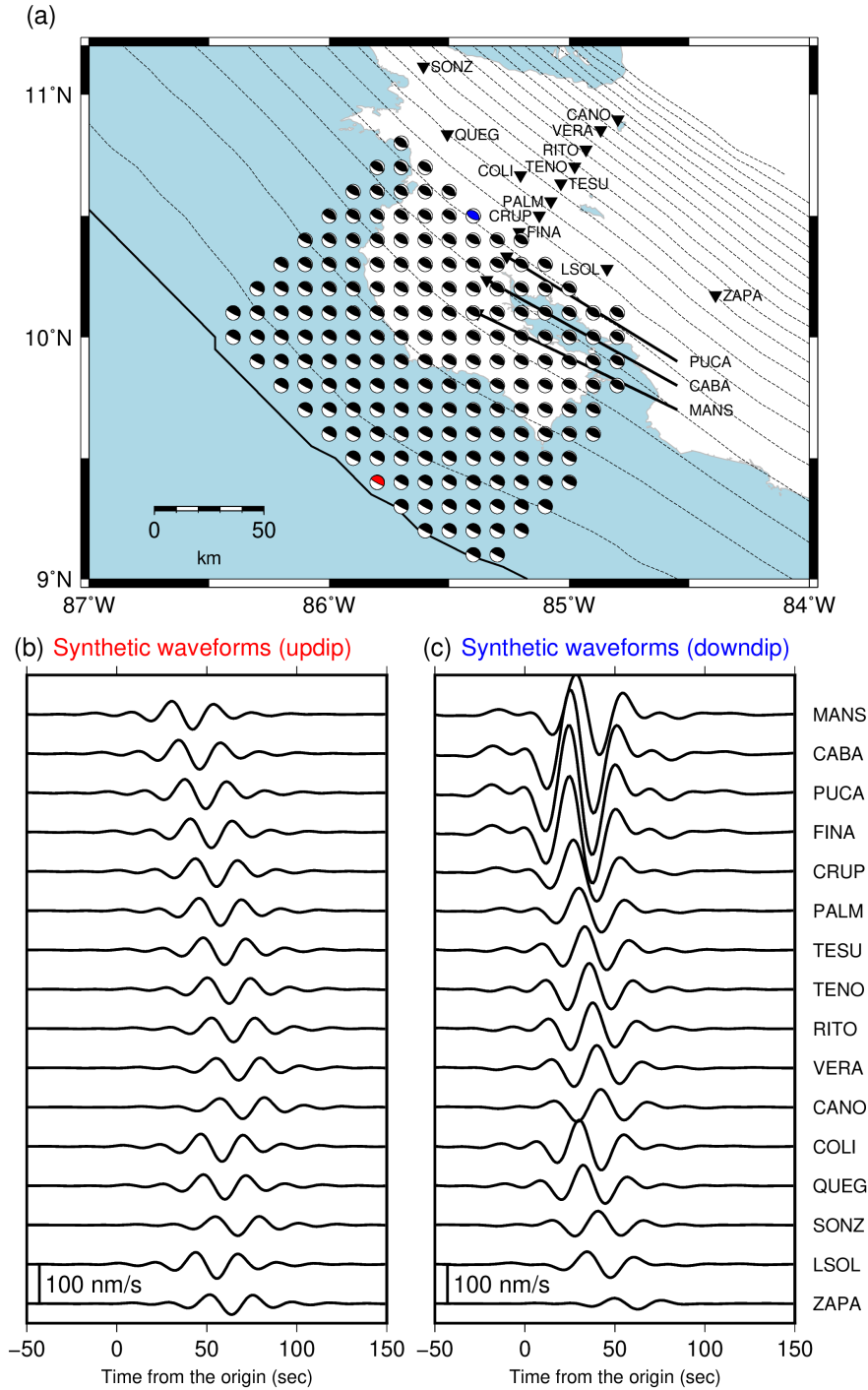
- 679 Scripps Institution of Oceanography. (1986). IRIS/IDA Seismic Network. International
680 Federation of Digital Seismograph Networks. <https://doi.org/10.7914/SN/II>
- 681 Shelly, D. R., Beroza, G. C., Ide, S., & Nakamura, S. (2006). Low-frequency earthquakes in
682 Shikoku, Japan, and their relationship to episodic tremor and slip. *Nature*, *442*(7099), 188–
683 191. <https://doi.org/10.1038/nature04931>
- 684 Shelly, D. R., Beroza, G. C., & Ide, S. (2007). Non-volcanic tremor and low-frequency
685 earthquake swarms. *Nature*, *446*(7133), 305–307. <https://doi.org/10.1038/nature05666>
- 686 Solomon, E. A., Kastner, M., Wheat, C. G., Jannasch, H., Robertson, G., Davis, E. E., & Morris,
687 J. D. (2009). Long-term hydrogeochemical records in the oceanic basement and forearc
688 prism at the Costa Rica subduction zone. *Earth and Planetary Science Letters*, *282*(1–4),
689 240–251. <https://doi.org/10.1016/j.epsl.2009.03.022>
- 690 Sugioka, H., Okamoto, T., Nakamura, T., Ishihara, Y., Ito, A., Obana, K., et al. (2012).
691 Tsunamigenic potential of the shallow subduction plate boundary inferred from slow
692 seismic slip. *Nature Geoscience*, *5*(6), 414–418. <https://doi.org/10.1038/ngeo1466>
- 693 Syracuse, E. M., van Keken, P. E., Abers, G. A., Suetsugu, D., Bina, C., Inoue, T., et al. (2010).
694 The global range of subduction zone thermal models. *Physics of the Earth and Planetary
695 Interiors*, *183*(1–2), 73–90. <https://doi.org/10.1016/j.pepi.2010.02.004>
- 696 Takagi, R., Uchida, N., & Obara, K. (2019). Along-Strike Variation and Migration of Long-
697 Term Slow Slip Events in the Western Nankai Subduction Zone, Japan. *Journal of
698 Geophysical Research: Solid Earth*, (Figure 1), 3853–3880.
699 <https://doi.org/10.1029/2018JB016738>
- 700 Takemura, S., Kobayashi, M., & Yoshimoto, K. (2017). High-frequency seismic wave
701 propagation within the heterogeneous crust: Effects of seismic scattering and intrinsic
702 attenuation on ground motion modelling. *Geophysical Journal International*, *210*(3), 1806–
703 1822. <https://doi.org/10.1093/gji/ggx269>
- 704 Takemura, S., Matsuzawa, T., Noda, A., Tonegawa, T., Asano, Y., Kimura, T., & Shiomi, K.
705 (2019). Structural Characteristics of the Nankai Trough Shallow Plate Boundary Inferred
706 From Shallow Very Low Frequency Earthquakes. *Geophysical Research Letters*, *46*(8),
707 4192–4201. <https://doi.org/10.1029/2019GL082448>
- 708 Takemura, S., Okuwaki, R., Kubota, T., Shiomi, K., Kimura, T., & Noda, A. (2020). Centroid
709 moment tensor inversions of offshore earthquakes using a three-dimensional velocity
710 structure model: slip distributions on the plate boundary along the Nankai Trough.
711 *Geophysical Journal International*, *222*(2), 1109–1125. <https://doi.org/10.1093/gji/ggaa238>
- 712 Tamaribuchi, K., Kobayashi, A., Nishimiya, T., Hirose, F., & Annoura, S. (2019).
713 Characteristics of Shallow Low-Frequency Earthquakes off the Kii Peninsula, Japan, in
714 2004 Revealed by Ocean Bottom Seismometers. *Geophysical Research Letters*, *46*(23),
715 13737–13745. <https://doi.org/10.1029/2019GL085158>
- 716 Uchida, N., & Matsuzawa, T. (2013). Pre- and postseismic slow slip surrounding the 2011
717 Tohoku-oki earthquake rupture. *Earth and Planetary Science Letters*, *374*, 81–91.
718 <https://doi.org/10.1016/j.epsl.2013.05.021>
- 719 Voss, N., Dixon, T. H., Liu, Z., Malservisi, R., Protti, M., & Schwartz, S. (2018). Do slow slip
720 events trigger large and great megathrust earthquakes? *Science Advances*, *4*(10), 1–6.
721 <https://doi.org/10.1126/sciadv.aat8472>
- 722 Voss, N. K., Malservisi, R., Dixon, T. H., & Protti, M. (2017). Slow slip events in the early part
723 of the earthquake cycle. *Journal of Geophysical Research: Solid Earth*, *122*(8), 6773–6786.
724 <https://doi.org/10.1002/2016JB013741>

- 725 Walter, J. I., Schwartz, S. Y., Protti, J. M., & Gonzalez, V. (2011). Persistent tremor within the
726 northern Costa Rica seismogenic zone. *Geophysical Research Letters*, *38*(1), 1–5.
727 <https://doi.org/10.1029/2010GL045586>
- 728 Walter, J. I., Schwartz, S. Y., Protti, M., & Gonzalez, V. (2013). The synchronous occurrence of
729 shallow tremor and very low frequency earthquakes offshore of the Nicoya Peninsula, Costa
730 Rica. *Geophysical Research Letters*, *40*(8), 1517–1522. <https://doi.org/10.1002/grl.50213>
- 731 Wang, L., & Barbot, S. (2020). Excitation of San Andreas tremors by thermal instabilities below
732 the seismogenic zone. *Science Advances*, *6*(36). <https://doi.org/10.1126/sciadv.abb2057>
- 733 Wessel, P., Smith, W. H. F., Scharroo, R., Luis, J., & Wobbe, F. (2013). Generic mapping tools:
734 Improved version released. *Eos*, *94*(45), 409–410. <https://doi.org/10.1002/2013EO450001>
- 735 Xie, S., Dixon, T. H., Malservisi, R., Jiang, Y., Protti, M., & Muller, C. (2020). Slow Slip and
736 Inter-transient Locking on the Nicoya Megathrust in the Late and Early Stages of an
737 Earthquake Cycle. *Journal of Geophysical Research: Solid Earth*, *125*(11), 1–22.
738 <https://doi.org/10.1029/2020JB020503>
- 739 Yabe, S., Tonegawa, T., & Nakano, M. (2019). Scaled Energy Estimation for Shallow Slow
740 Earthquakes. *Journal of Geophysical Research: Solid Earth*, *124*(2), 1507–1519.
741 <https://doi.org/10.1029/2018JB016815>
- 742 Yabe, S., Baba, S., Tonegawa, T., Nakano, M., & Takemura, S. (2021). Seismic energy radiation
743 and along-strike heterogeneities of shallow tectonic tremors at the Nankai Trough and Japan
744 Trench. *Tectonophysics*, 228714. <https://doi.org/10.1016/j.tecto.2020.228714>
- 745 Yao, S., & Yang, H. (2020). Rupture Dynamics of the 2012 Nicoya Mw 7.6 Earthquake:
746 Evidence for Low Strength on the Megathrust. *Geophysical Research Letters*, *47*(13), 1–11.
747 <https://doi.org/10.1029/2020GL087508>
- 748 Yokota, Y., & Ishikawa, T. (2020). Shallow slow slip events along the Nankai Trough detected
749 by GNSS-A. *Science Advances*, *6*(3), 1–12. <https://doi.org/10.1126/sciadv.aay5786>
- 750 Yoshimoto, K., Sato, H., & Ohtake, M. (1993). Frequency-Dependent Attenuation of P and S
751 Waves In the Kanto Area, Japan, Based On the Coda-Normalization Method. *Geophysical*
752 *Journal International*, *114*(1), 165–174. [https://doi.org/10.1111/j.1365-](https://doi.org/10.1111/j.1365-246X.1993.tb01476.x)
753 [246X.1993.tb01476.x](https://doi.org/10.1111/j.1365-246X.1993.tb01476.x)
- 754 Yue, H., Lay, T., Schwartz, S. Y., Rivera, L., Protti, M., Dixon, T. H., et al. (2013). The 5
755 September 2012 Nicoya, Costa Rica Mw 7.6 earthquake rupture process from joint
756 inversion of high-rate GPS, strong-motion, and teleseismic P wave data and its relationship
757 to adjacent plate boundary interface properties. *Journal of Geophysical Research: Solid*
758 *Earth*, *118*(10), 5453–5466. <https://doi.org/10.1002/jgrb.50379>

759 **Figures**

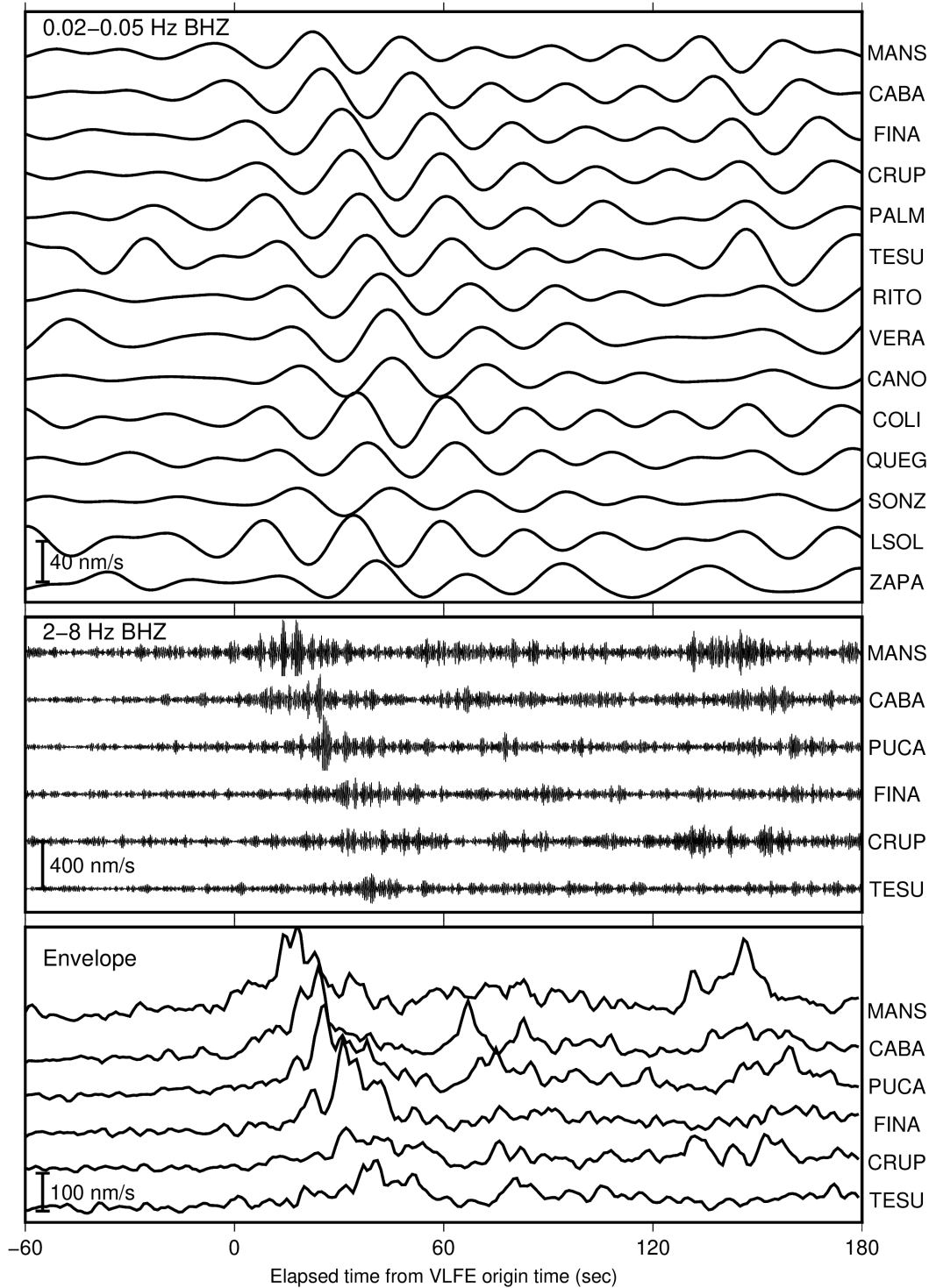
760

761 **Figure 1.** (a) Large regular and slow earthquake areas based on previous studies around the Nicoya
 762 Peninsula, in Costa Rica. Green contours show the coseismic slip distribution of the 2012 Mw 7.6
 763 earthquake with a 1-m interval (Yue et al., 2013). Blue and dark blue areas show the slip areas of
 764 large and tsunami earthquakes (1990 Mw 7.3: Protti et al., 1995; others: Yue et al., 2013). Orange
 765 ellipses with dashed lines show large slip areas of the 2007 SSE (Jiang et al., 2017). The orange
 766 ellipse with a solid line shows the distributions of LFEs (Brown et al., 2009) and tremors
 767 (Outerbridge et al., 2010). The purple polygon shows the area whose afterslip of the 2012 Mw 7.6
 768 earthquake is more than 150 mm (Malvervisi et al., 2015). Black inverted triangles show the station
 769 locations of the TUCAN network used in VLFE detection (Section 2.2). Dashed contours indicate
 770 the isodepths of the top of the Cocos Plate with 10 km intervals (Slab2; Hayes et al., 2018). (b)
 771 Map of the Central American subduction zone. Solid line represents the Middle America Trench
 772 (Slab2; Hayes et al., 2018). Dashed contours are the same as (a). Black arrow indicates the
 773 convergence direction of the Cocos Plate, which subducts below the Caribbean plate from the
 774 Middle America Trench (NUVEL-1A; DeMets et al., 1994). Inverted triangles show the locations
 775 of stations of the TUCAN network. Brown triangles are stations which were used in beamforming
 776 (Section 2.3). The black lines in the inset show plate boundaries.



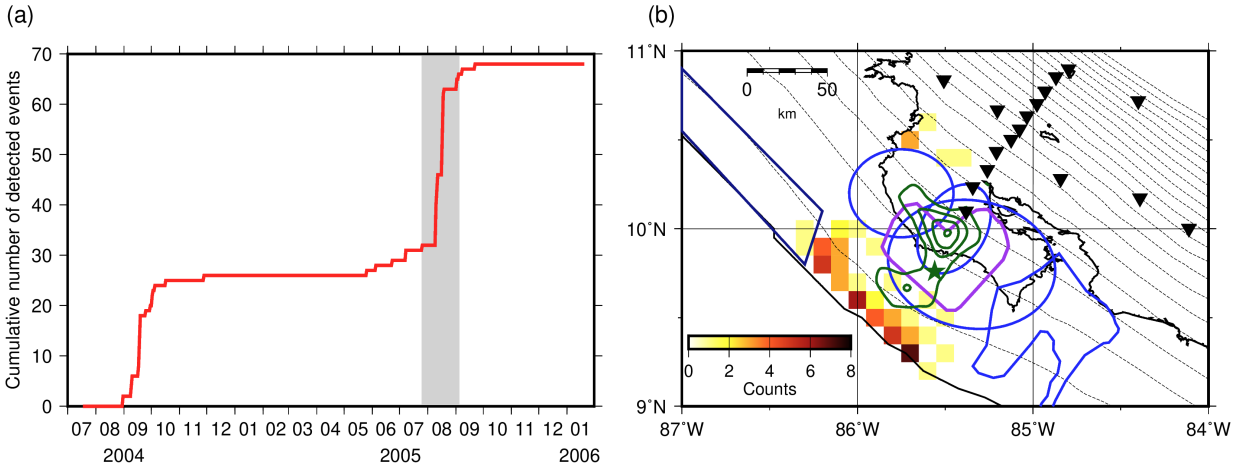
777

778 **Figure 2.** (a) Virtual source grids assumed in this study. Beach balls show the locations and focal
 779 mechanisms of the virtual sources. Inverted triangles and the black line are the same as in Figure
 780 1. Dashed contours indicate the isodepths of the top of the Cocos Plate with 10 km intervals (Slab2;
 781 Hayes et al., 2018). Examples of waveforms of virtual sources in the (b) updip and (c) downdip
 782 areas. Sources of Figures 1b and 1c are shown by the red and blue beachballs in Figure 2a,
 783 respectively.



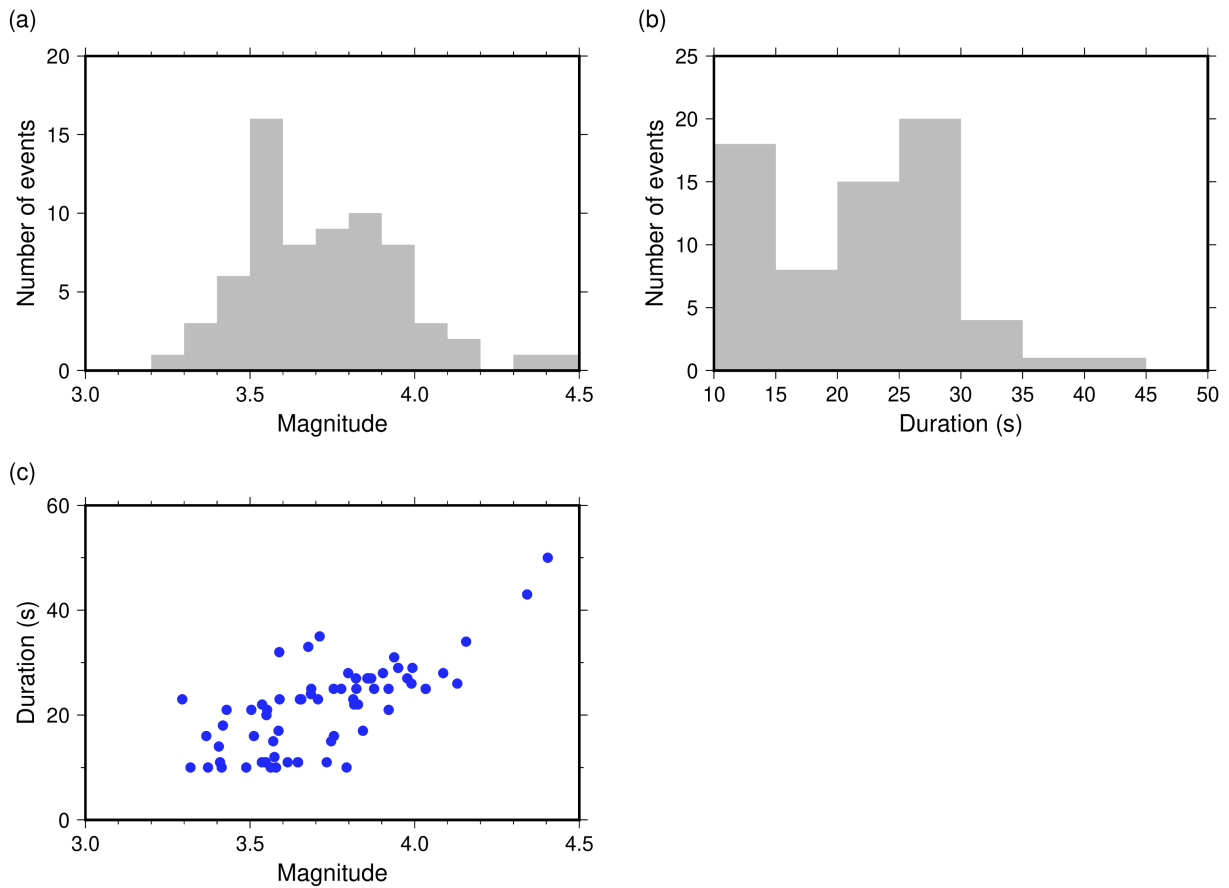
784

785 **Figure 3.** Example of waveforms of a VLFE and the corresponding tremor located at 85.8°W and
 786 9.4°N (shown by a red beachball in Figure 2a) in the frequency range of 0.02–0.05 Hz and 2–8 Hz,
 787 and smoothed root-mean-square envelope in the frequency range of 2–8 Hz. Seismograms are
 788 shown from the origin time of the VLFE, 03:53:47 (UTC), August 10, 2005.



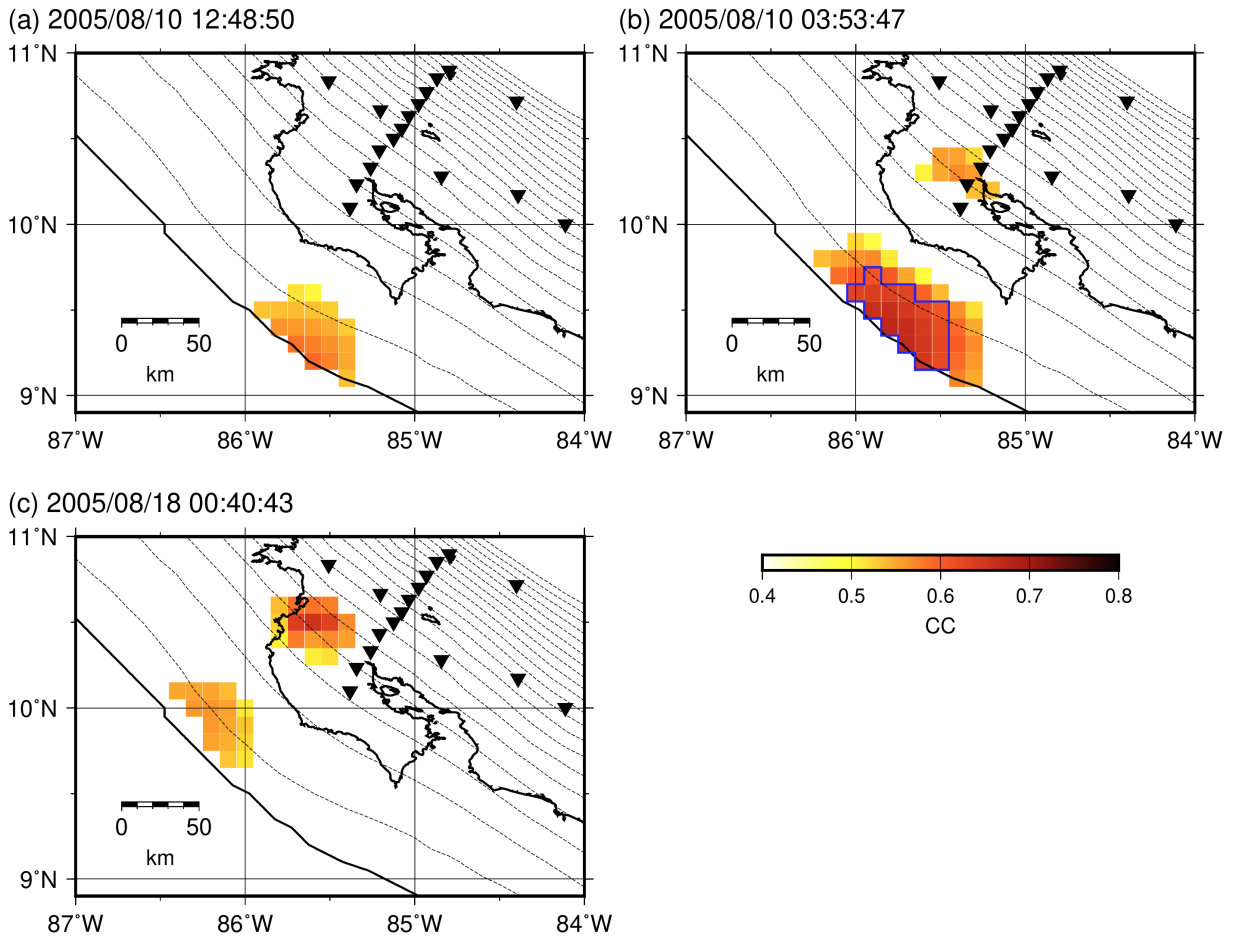
789

790 **Figure 4.** (a) Cumulative number of the VLFs from July 2004 to January 2006. Gray shading
 791 shows the period of the 2005 SSE (Jiang et al., 2012). (b) Distribution of the number of detected
 792 events at each virtual source. Blue ellipses and polygons, dark blue quadrangle, inverted triangles,
 793 black line, the purple polygon, and dashed contours are the same as in Figure 1.



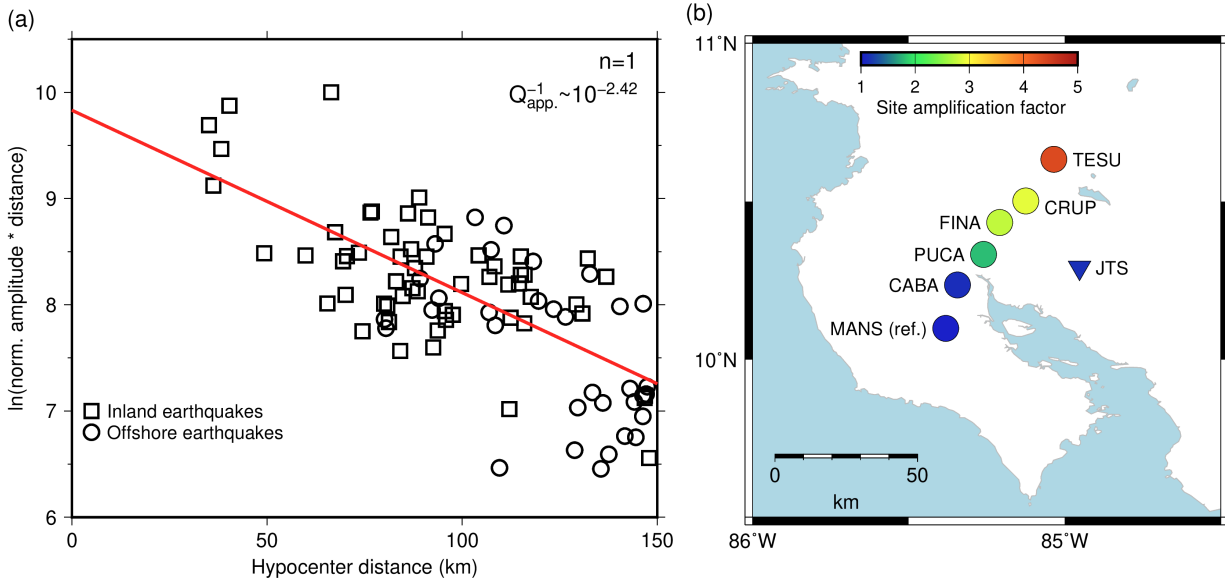
794

795 **Figure 5.** Distribution of (a) magnitudes and (b) source durations of VLFs. (c) Relationship
 796 between source durations and magnitudes of VLFs.



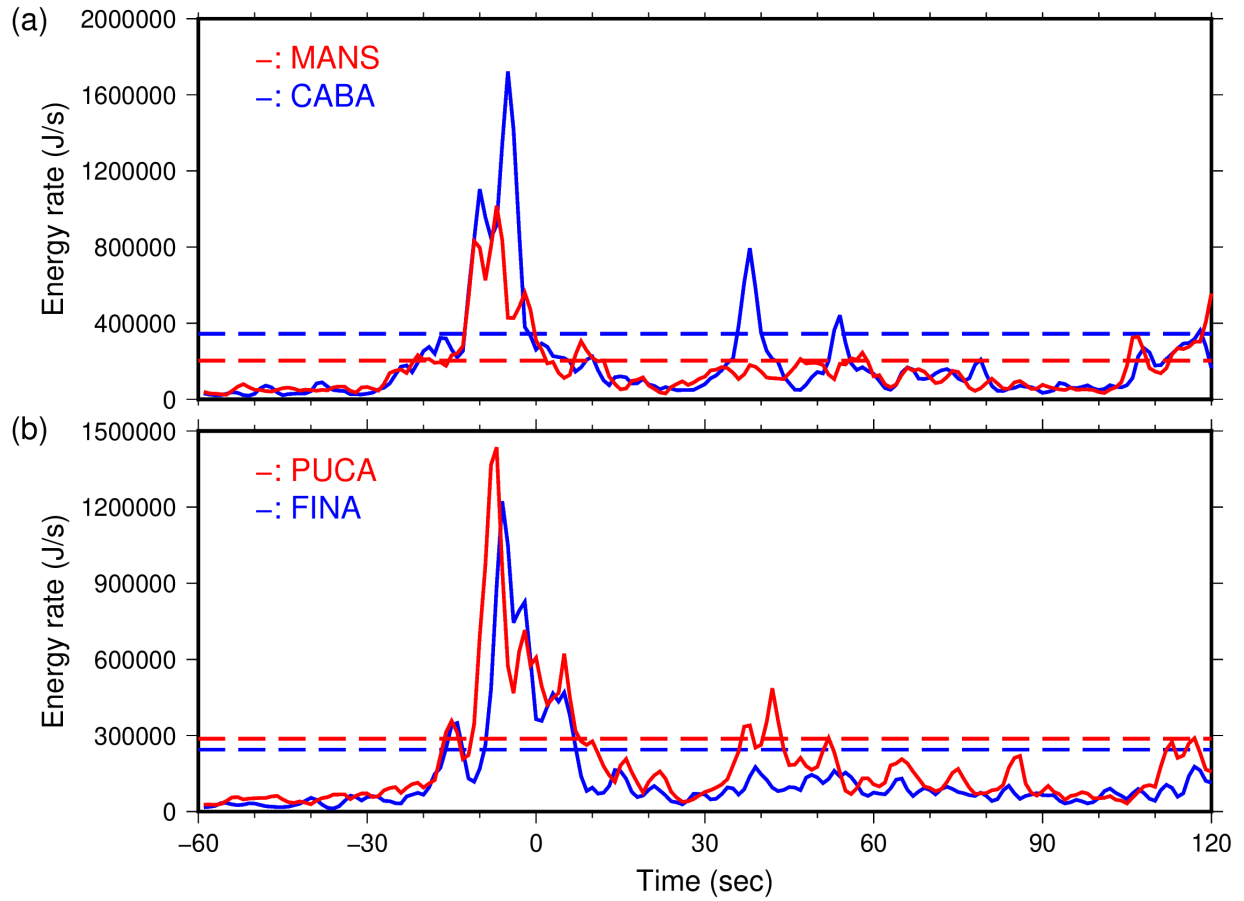
797

798 **Figure 6.** Examples of CC distributions of (a) an event which has large CCs only in updip grids,
 799 (b) an event which has large CCs both in updip and downdip grids but is located in an updip grid,
 800 and (c) an event which has large CCs both in updip and downdip grids but is located in a downdip
 801 grid. Inverted triangles, black line, and dashed contours are the same as in Figure 1. The blue
 802 polygon in (b) indicates the grids whose CC are more than 0.9 times of the maximum CC.



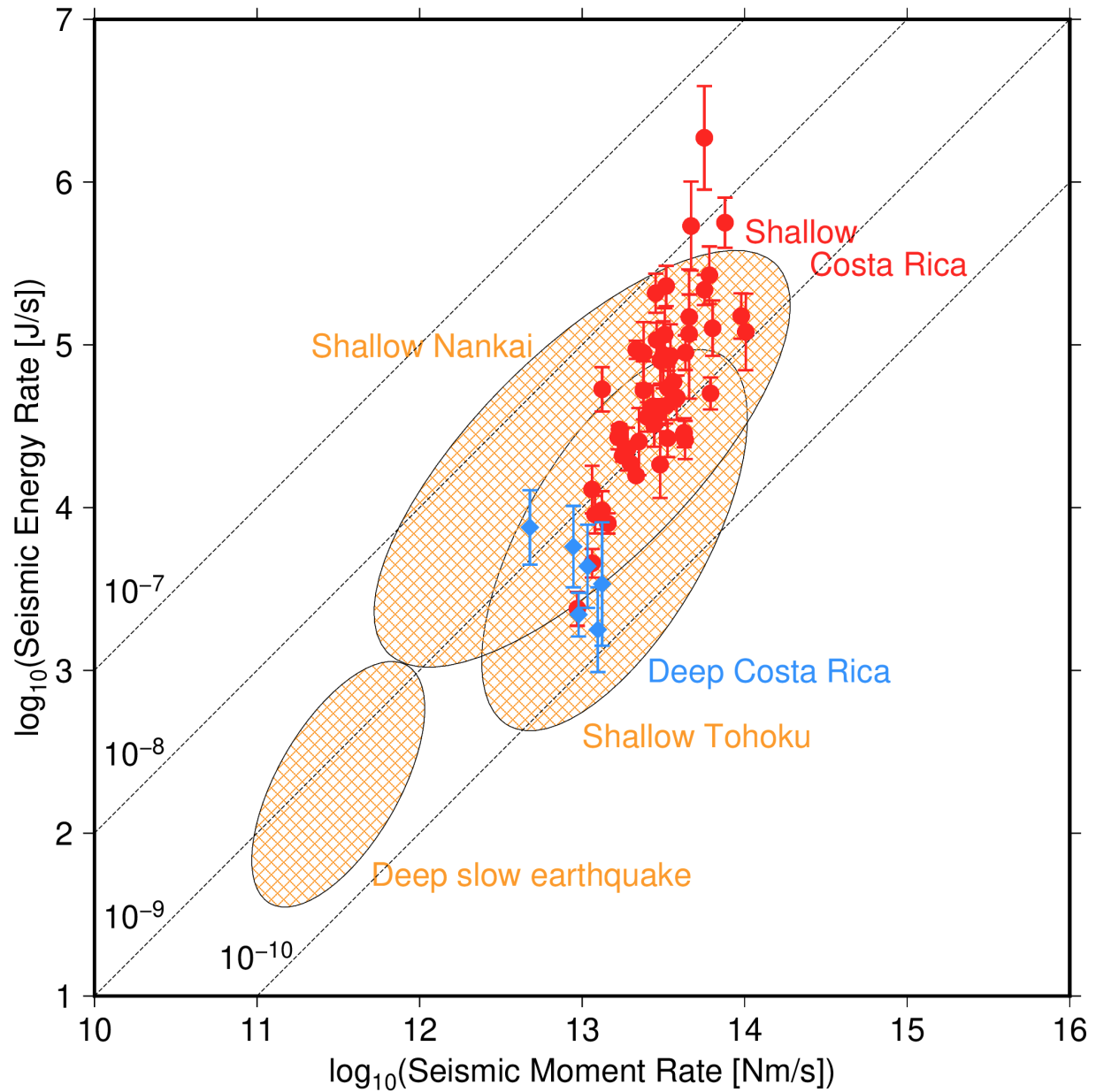
803

804 **Figure 7.** (a) Relationship between logarithm of coda-normalized maximum *S*-wave amplitudes
 805 and hypocentral distances. To eliminate effects of geometrical spreading of *S*-wave, coda-
 806 nomadized *S*-wave amplitudes were multiplied by their hypocentral distance. Red line shows the
 807 regression line using Equation (2). (b) Site amplification factors relative to MANS based on
 808 relative coda amplitude measurements.



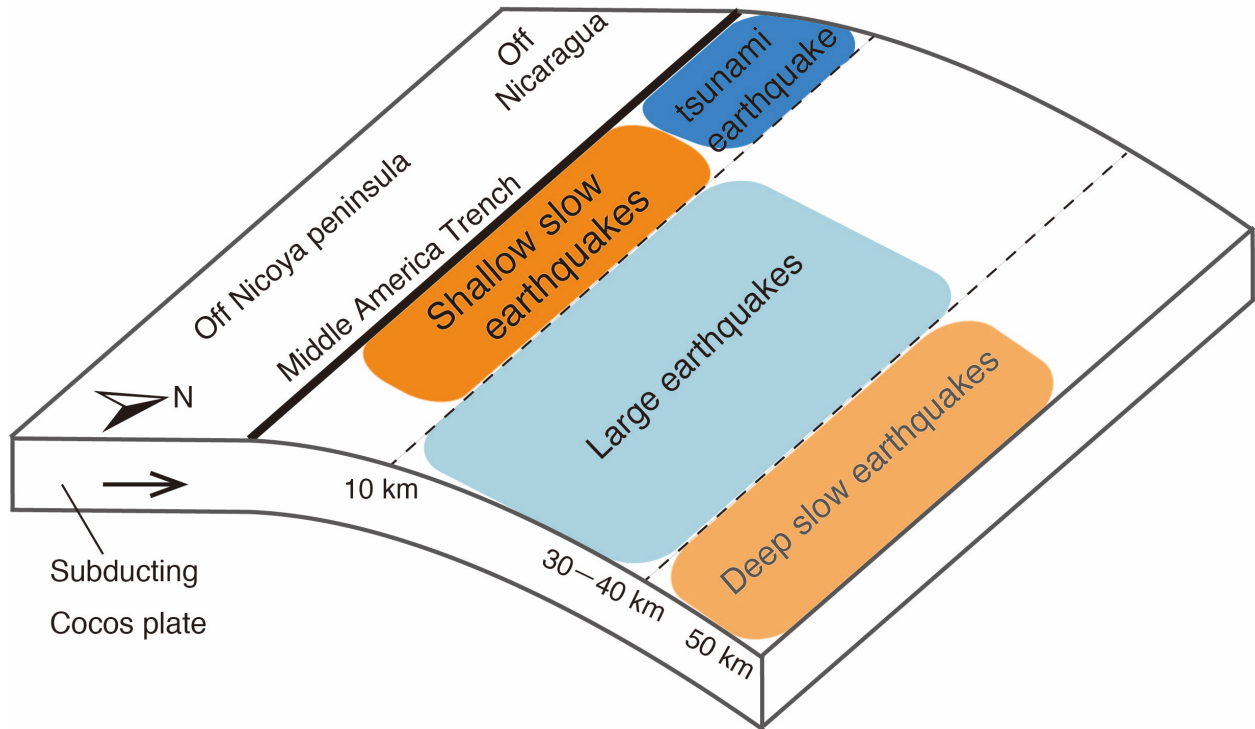
809

810 **Figure 8.** Temporal changes of energy rate functions of a tremor in (a) MANS and CABA and (b)
 811 PUCA and FINA. The corresponding VLFE occurs on 03:53:47 (UTC), August 10, 2012. Dashed
 812 lines indicate the threshold, which is set as 20% of the maximum value of the energy rate functions.



813

814 **Figure 9.** Relationship between seismic moment rates of VLFs and seismic moment rates of
 815 tremors estimated in this study. Red circles and blue diamonds show the events of updip and
 816 downdip regions, respectively. Dashed lines show scaled energies of 10^{-7} , 10^{-8} , 10^{-9} , and 10^{-10} .
 817 Orange shadings show the relationships between seismic moment rates of VLFs and seismic
 818 moment rates of tremors of shallow slow earthquakes in the Nankai (Yabe et al., 2019) and Tohoku
 819 subduction zones (Yabe et al., 2021), and deep slow earthquakes in southwest Japan (Ide & Yabe,
 820 2014), Cascadia (Ide, 2016), and Mexico (Ide & Maury, 2018). We note that scaled energies of
 821 shallow slow earthquakes were estimated for individual events, whereas those of deep slow
 822 earthquakes were estimated for stacked events.



823

824 **Figure 10.** A schematic illustration showing the interpretation of distributions of slow, tsunami,
825 and large regular earthquakes in the Central American subduction zone. The areas of large
826 earthquakes, the 1992 tsunami earthquake, and deep slow earthquakes are referred from Yue et al.
827 (2013), Satake (1994), and Outerbridge et al. (2010), respectively.

828

829